

ACCEPTED MANUSCRIPT



Identification of a Munc13-sensitive step in chromaffin cell large dense-core vesicle exocytosis

Kwun-nok Mimi Man, Cordelia Imig, Alexander Matthias Walter, Paulo S Pinheiro, David R Stevens, Jens Rettig, Jakob B Sørensen, Benjamin H Cooper, Nils Brose, Sonja M Wojcik

DOI: <http://dx.doi.org/10.7554/eLife.10635>

Cite as: eLife 2015;10.7554/eLife.10635

Received: 5 August 2015

Accepted: 16 November 2015

Published: 17 November 2015

This PDF is the version of the article that was accepted for publication after peer review. Fully formatted HTML, PDF, and XML versions will be made available after technical processing, editing, and proofing.

Stay current on the latest in life science and biomedical research from eLife.
[Sign up for alerts](http://elifesciences.org) at elifesciences.org

1 **Identification of a Munc13-sensitive step in chromaffin cell large**
2 **dense-core vesicle exocytosis**

3 Kwun-nok M. Man¹, Cordelia Imig¹, Alexander M. Walter², Paulo S.
4 Pinheiro³, David R. Stevens⁴, Jens Rettig⁴, Jakob B. Sørensen³, Benjamin
5 H. Cooper¹, Nils Brose¹, and Sonja M. Wojcik¹.

6

7 ¹Department of Molecular Neurobiology, Max Planck Institute of Experimental
8 Medicine, D-37075 Göttingen, Germany

9 ²Leibniz Institute for Molecular Pharmacology, D-13125 Berlin, Germany

10 ³Department of Neuroscience and Pharmacology, Faculty of Health and Medical
11 Sciences and Lundbeck Foundation Center for Biomembranes in Nanomedicine,
12 University of Copenhagen, 2200N Copenhagen, Denmark

13 ⁴Department of Physiology, Saarland University, D-66421 Homburg, Saar, Germany

14 Contact: wojcik@em.mpg.de

15 [Tel: +49 551 3899 722](tel:+495513899722)

16 [Fax: +49 551 3899 715](tel:+495513899715)

17

18 Short title: Munc13s in LDCV Priming and Docking

19

20 **Abstract**

21 It is currently unknown whether the molecular steps of large dense-core vesicle
22 (LDCV) docking and priming are identical to the corresponding reactions in synaptic
23 vesicle (SV) exocytosis. Munc13s are essential for SV docking and priming, and we
24 systematically analyzed their role in LDCV exocytosis using chromaffin cells lacking
25 individual isoforms. We show that particularly Munc13-2 plays a fundamental role in
26 LDCV exocytosis, but in contrast to synapses lacking Munc13s, the corresponding
27 chromaffin cells do not exhibit a vesicle docking defect. We further demonstrate that
28 ubMunc13-2 and Munc13-1 confer Ca^{2+} -dependent LDCV priming with similar
29 affinities, but distinct kinetics. Using a mathematical model, we identify an early
30 LDCV priming step that is strongly dependent upon Munc13s. Our data demonstrate
31 that the molecular steps of SV and LDCV priming are very similar while SV and
32 LDCV docking mechanisms are distinct.

33

34 **Introduction**

35 The regulated, Ca^{2+} -triggered secretion of catecholamines from chromaffin cell
36 LDCVs is an integral part of the physiological adaptation to environmental stressors.
37 Like the exocytosis of neuronal SVs, LDCV exocytosis is mediated by SNARE
38 complex formation, in concert with Ca^{2+} sensors and essential regulatory proteins
39 (James and Martin, 2013; Neher, 2006; Ovsepian and Dolly, 2011; Pang and Sudhof,
40 2010).

41 Mammalian uncoordinated 13 (Munc13) proteins are essential SV priming factors in
42 neurons (Augustin et al., 1999; Richmond et al., 1999; Rosenmund et al., 2002), and
43 ultrastructural studies have shown that in synapses lacking Munc13s/Unc-13, SVs
44 also fail to physically dock to synaptic active zones (Imig et al., 2014; Siksou et al.,
45 2009; Weimer et al., 2006). At the molecular level, this morphological phenotype
46 most likely corresponds to a role of Munc13s in mediating the formation of SNARE
47 complexes at vesicular release sites (Hammarlund et al., 2007; Hammarlund et al.,
48 2008; Imig et al., 2014; Ma et al., 2011; Ma et al., 2013; Yang et al., 2015).

49 The Munc13 family consists of five members, Munc13-1 (*Unc13a*), Munc13-2
50 (*Unc13b*), Munc13-3 (*Unc13c*), the brain specific angiogenesis inhibitor I-associated
51 protein 3 (*Baiap3*), and the non-neuronal isoform Munc13-4 (*Unc13d*) (Koch et al.,
52 2000). Genetic deletion of *Unc13a* and *Unc13b* completely eliminates SV exocytosis
53 in hippocampal neurons (Varoqueaux et al., 2002), and selectively reduces synaptic
54 vs. extrasynaptic exocytosis of neuronal LDCVs (van de Bospoort et al., 2012), which
55 indicates that SV and LDCV exocytosis at active zones is mediated by similar
56 molecular mechanisms. By contrast, studies in *C. elegans* and *Drosophila* have shown
57 that Unc-13/dUnc-13 selectively regulate SV release, whereas the Ca^{2+} -dependent

58 activator proteins for secretion (CAPS/Unc-31) specifically regulate LDCV release
59 (Hammarlund et al., 2008; Renden et al., 2001; Speese et al., 2007; Zhou et al., 2007).

60 In mammals, Munc13s and CAPSs appear to perform non-redundant functions critical
61 for both SV and LDCV exocytosis in neurons (Jockusch et al., 2007; van de Bospoort
62 et al., 2012), as well as for LDCV exocytosis in neuroendocrine cells (Elhamdani et
63 al., 1999; Kabachinski et al., 2014; Kang et al., 2006; Kwan et al., 2006; Liu et al.,
64 2010; Liu et al., 2008; Speidel et al., 2008). Yet, to date, while CAPS-1 and CAPS-2
65 have been shown to be required for LDCV exocytosis in mammalian chromaffin cells
66 (Liu et al., 2010; Liu et al., 2008), evidence that endogenous Munc13s are required
67 for LDCV exocytosis is lacking. In fact, the role of Munc13-1 and ubMunc13-2 has
68 only been examined in the context of overexpression studies, and other isoforms have
69 not been investigated (Ashery et al., 2000; Bauer et al., 2007; Liu et al., 2010; Stevens
70 et al., 2005; Zikich et al., 2008).

71 In the present study, we performed the first comprehensive analysis of all neuronal
72 and neuroendocrine members of the Munc13 protein family in chromaffin cells,
73 defining their respective roles in LDCV exocytosis. We identify the Ca^{2+} -dependent
74 step in the priming process at which Munc13-1 and ubMunc13-2 operate, and
75 demonstrate that, although they are critical for LDCV priming and release, LDCV
76 docking can occur without them.

77

78 **Results**

79 **Expression of Munc13 isoforms in the mouse adrenal gland**

80 We first analyzed the expression of all Munc13 isoforms in the murine adrenal gland
81 by Western blotting (Figure 1). In perinatal adrenal glands, we detected Munc13-1
82 (Figure 1A and Figure 1–figure supplement 1B), the ubiquitous isoform ubMunc13-2
83 (Figure 1B and Figure 1–figure supplement 1B), and Baiap3 (Figure 1D). Not
84 detected were the brain-specific isoform of Munc13-2 (bMunc13-2), which is a splice
85 variant expressed from the same gene as ubMunc13-2 (Figure 1B), Munc13-3 (Figure
86 1C), and the non-neuronal isoform Munc13-4 (Figure 1E). To directly compare the
87 expression levels of Munc13-1, ubMunc13-2, bMunc13-2, and Munc13-3, we used
88 knockin mice that express these proteins fused to enhanced yellow or green
89 fluorescent protein (EYFP/EGFP) from the respective endogenous loci (Cooper et al.,
90 2012; Kalla et al., 2006). We found that ubMunc13-2-EYFP is the only isoform
91 readily detectable in the adrenal gland using an antibody to the GFP-derived tags
92 (Figure 1–figure supplement 1A).

93 To assess whether the isoforms detected in whole gland homogenates are present in
94 the adrenal medulla, and/or the adrenal cortex, we dissected adult wild-type (WT)
95 adrenal glands, and used an antibody to the LDCV marker Chromogranin A (CgA) to
96 monitor effective separation of the medullary tissue, which consists mostly of
97 chromaffin cells, from cortical tissue (Figure 1F). The expression of Munc13-1 and
98 Baiap3 in the adrenal gland is largely restricted to the medulla. Expression of
99 ubMunc13-2 was detected in both adrenal medulla and cortex. Thus, a significant
100 fraction of the ubMunc13-2 signal detected in whole gland homogenates (Figure 1B)

101 appears to originate from the adrenal cortex, possibly due to innervation of the cortex
102 by ubMunc13-2 positive synapses.

103

104 **Absence of Munc13-1, Munc13-3, or Baiap3 does not impair LDCV exocytosis in**
105 **chromaffin cells**

106 Next, we analyzed cultured chromaffin cells from knockout (KO) mice deficient for
107 the individual Munc13 isoforms (Figure 2). LDCV exocytosis was triggered using
108 flash photolysis of caged Ca^{2+} , which causes a sharp global increase in intracellular
109 $[\text{Ca}^{2+}]$ (Neher, 2006). Fusion of LDCVs with the plasma membrane was monitored by
110 measurement of the membrane capacitance change (ΔCm). Fitting a sum of three
111 exponentials to the exocytotic burst of each individual trace identifies the amplitudes
112 and time constants of release, which are generally interpreted as two kinetically
113 distinct vesicle pools, the fast burst as the Readily-Releasable Pool (RRP), and the
114 slow burst as the Slowly-Releasable Pool (SRP) (Sorensen et al., 2003a; Voets, 2000).
115 However, as will be discussed later, the slow burst component may in fact not be a
116 releasable pool, but instead represent the conversion from a Non-Releasable Pool
117 (NRP), to the RRP (Walter et al., 2013). The rate of sustained release was measured
118 as a linear component after the exocytotic burst, and reflects the ongoing recruitment
119 of LDCVs into the NRP/SRP and RRP. Deletion of Munc13-1 (*Unc13a*), the major
120 Munc13 isoform in SV exocytosis (Augustin et al., 1999; Varoqueaux et al., 2002),
121 did not markedly alter LDCV exocytosis compared to WT littermate controls (Figure
122 2A,D), nor did it affect the kinetics of the exocytotic burst (Figure 2D).

123 Although we did not detect Munc13-3 in the adrenal gland, we wanted to rule out
124 possible physiological effects of protein expression below the detection limit of

125 Western blot analysis (Figure 1C), and included *Unc13c*^{KO} mice in our analysis.
126 However, as expected, LDCV exocytosis in *Unc13c*^{KO} chromaffin cells was not
127 perturbed (Figure 2B,D).

128 We then investigated the possible role of Baiap3 in LDCV exocytosis, as this isoform
129 is prominently expressed in the adrenal medulla (Figure 1D,F). Surprisingly, LDCV
130 exocytosis in *Baiap3*^{KO} cells was intact (Figure 2C,D). Furthermore, *Baiap3*^{KO} cells
131 also did not show a release deficit when we stimulated the cells using a series of
132 depolarization steps (Figure 2-figure supplement, 1A-C), nor did overexpression of
133 Baiap3 in WT cells affect LDCV exocytosis (Figure 2-figure supplement 1D-F).

134

135 **Absence of ubMunc13-2 dramatically reduces LDCV release**

136 We then analyzed the role of ubMunc13-2 and Munc13-1 in chromaffin cell LDCV
137 exocytosis. For this purpose, we used an *Unc13a/b* (DKO) mouse line. Heterozygous
138 (Het) animals of this line express ~50 % of WT levels of Munc13-1 and Munc13-2,
139 which does not affect neurotransmission (Augustin et al., 1999; Varoqueaux et al.,
140 2002). Data were collected from genotype groups available for a given litter and were
141 pooled for analysis. Because our breeding scheme did not produce littermate WT
142 animals in sufficient numbers, and because deletion of *Unc13a* alone was without
143 effect, data from *Unc13a*^{WT}*Unc13b*^{Het} and *Unc13a*^{Het}*Unc13b*^{Het} cells were pooled and
144 used as control (Figure 2E-J, *Unc13a*^{WT/Het}*Unc13b*^{Het}).

145 Deletion of both *Unc13a* alleles together with a single *Unc13b* allele
146 (*Unc13a*^{KO}*Unc13b*^{Het}) did not reduce LDCV release (Figure 2E,F). By contrast,
147 abrogation of ubMunc13-2 expression alone, irrespective of the *Unc13a* genotype,

148 drastically diminished release (Figure 2E,F). Furthermore, in the context of the
149 *Unc13b*^{KO} background, cells with *Unc13a*^{WT}, *Unc13a*^{Het}, and *Unc13a*^{KO} genotypes
150 showed a progressive reduction of LDCV release that depended on the number of
151 *Unc13a* alleles present (Figure 2F,G). The fast and slow burst components were
152 reduced to 39%, 32%, and 27%, and to 54%, 52%, and 42% of control levels,
153 respectively (Figure 2F). The rate of sustained release was reduced even more
154 dramatically, to 26%, 19%, and 12% of control levels (Figure 2F). When one uses the
155 *Unc13a*^{WT}*Unc13b*^{KO} genotype as a reference point (Figure 2G), the deletion of
156 *Unc13a* caused a reduction of the sustained release component to 48%. The rate of
157 sustained release of *Unc13a*^{KO}*Unc13b*^{KO} cells was also significantly reduced when
158 compared to *Unc13a*^{Het}*Unc13b*^{KO} cells.

159 The deletion of both *Unc13a* and *Unc13b* significantly delayed the onset of vesicular
160 exocytosis triggered by flash photolysis, compared to control and
161 *Unc13a*^{KO}*Unc13b*^{Het} cells (Figure 2H). *Unc13a*^{WT}*Unc13b*^{KO} cells also showed a mild
162 increase in delay. However, this difference was significant only when compared to
163 *Unc13a*^{KO}*Unc13b*^{Het} cells, but not compared to the other groups.

164 Thus, ubMunc13-2, the only isoform expressed from the *Unc13b* gene in mouse
165 chromaffin cells, is the most critical isoform for LDCV release in this cell type.
166 Moreover, in its absence it becomes apparent that endogenous Munc13-1 also
167 regulates LDCV release in this cell type.

168

169

170

171 **Reduced IRP and RRP in the absence of ubMunc13-2**

172 We next assessed whether ubMunc13-2 affects LDCV release in response to Ca^{2+}
173 entry through voltage-gated Ca^{2+} channels by stimulating the cells with a series of
174 depolarization steps (Figure 3). The first six short depolarizations of the train release
175 the Immediately-Releasable Pool (IRP), i.e. the subset of RRP vesicles located closest
176 to Ca^{2+} -channels (Schonn et al., 2010; Voets et al., 1999). We found a significant
177 reduction in LDCV release; the size of the RRP in *Unc13b*^{KO} cells was reduced to
178 53% of WT levels (Figure 3C). This deficit is somewhat less pronounced than the
179 reduction seen in the flash photolysis experiment (reduction to 39%, Figure 2F), most
180 likely because the depolarization protocol used to obtain the data shown in Figure 3
181 lasts several seconds and therefore causes some ongoing recovery of the RRP. By
182 contrast, in flash photolysis experiments, the RRP is probed within ~60 ms (3 times
183 the time constant), which is much faster than the recovery of the RRP. Strikingly, in
184 the depolarization experiment, impaired release in *Unc13b*^{KO} cells was already
185 evident in response to the first 10-ms depolarization (Figure 3B), which implies that
186 lack of ubMunc13-2 would even affect resting level catecholamine release driven by
187 low frequency stimulation (Zhou and Mislser, 1995).

188

189 **Reduced catecholamine release in the absence of ubMunc13-2**

190 To understand how ubMunc13-2 affects the kinetics of single catecholamine release
191 events, we performed single spike amperometry while infusing the cells with a
192 solution with moderate (~4.6 μM) $[\text{Ca}^{2+}]$ (Figure 4). *Unc13b*^{KO} cells showed a
193 dramatic reduction in spike frequency (Figure 4B,C), whereas basic spike parameters
194 such as duration, half-width, maximum amplitude, charge, rise time, and decay time

195 were unchanged (Figure 4D-I). Amplitude, duration and charge of the spike foot
196 signal, which is thought to reflect release during the initial formation of the fusion
197 pore prior to full fusion, were also unchanged (Figure 4J-L). However, we found that
198 the number of spikes that did show these foot signals was slightly reduced in
199 *Unc13b*^{KO} cells (Figure 4M), which may indicate that fusion pore dynamics are
200 altered for some release events. However, overall, the LDCVs undergoing fusion in
201 the absence of ubMunc13-2 do so without major alterations in fusion kinetics or
202 vesicle content.

203

204 **Munc13 isoforms display different LDCV priming efficiencies**

205 As our experiments so far showed that, with the exception of Baiap3, the contribution
206 of the Munc13 isoforms to the regulation of LDCV release correlates with their level
207 of expression in perinatal adrenal glands, we next wanted to compare the intrinsic
208 properties of the different isoforms. To this end, we overexpressed Munc13-1,
209 ubMunc13-2, Baiap3, and its closest relative Munc13-4 using Semliki Forest Virus
210 (SFV) in *Unc13a*^{KO}*Unc13b*^{KO} cells. Munc13-1 and ubMunc13-2 were expressed as
211 EGFP fusion constructs whose functions are identical to those of the respective WT
212 proteins (Rosenmund et al., 2002), whereas Baiap3 and Munc13-4 were expressed as
213 internal ribosome entry site (IRES)-EGFP constructs, to avoid possible confounding
214 effects of a fusion tag. *Unc13a*^{KO}*Unc13b*^{KO} cells expressing only EGFP were used as
215 control. For the purpose of comparison, the averaged traces obtained from the rescue
216 experiments with the four isoforms were plotted in the same graph (Figure 5A). The
217 exocytotic burst was measured as the ΔC_m within the first 0.5 s after the flash
218 stimulus, and the rate of sustained release was measured as the ΔC_m between 0.5 s

219 and 4 s after the flash (Figure 5B). Interestingly, Munc13-1 and ubMunc13-2 were
220 both able to rescue the LDCV release deficit of *Unc13a*^{KO}*Unc13b*^{KO} cells (Figure
221 5A,B). However, rescue with ubMunc13-2 resulted in an enormous enhancement of
222 LDCV exocytosis to levels that by far exceeded the amount of exocytosis typical of
223 WT cells, for both the exocytotic burst and the rate of sustained release (Figure
224 5A,B). The direct comparison of Munc13-1 and ubMunc13-2 expressing cells with
225 matching EGFP fluorescence intensity confirmed that the stronger enhancement of
226 burst size and rate of sustained release in ubMunc13-2 expressing cells was not due to
227 higher expression levels of ubMunc13-2 (Figure 5–figure supplement 1).

228 Overexpression of Baiap3 failed to rescue the LDCV release deficit of the
229 *Unc13a*^{KO}*Unc13b*^{KO} chromaffin cells (Figure 5A,B). Yet, its closest relative,
230 Munc13-4, which regulates SNARE-mediated vesicular exocytosis in the
231 hematopoietic system (Feldmann et al., 2003; Shirakawa et al., 2004), was able to
232 rescue LDCV exocytosis in *Unc13a*^{KO}*Unc13b*^{KO} cells, albeit less efficiently than
233 Munc13-1 or ubMunc13-2 (Figure 5A,B). To exclude the possibility that these
234 findings might be due to inefficient translation of Baiap3 and Munc13-4, protein
235 expression was confirmed with isoform-specific antibodies in SFV-infected neuronal
236 cultures, which provide enough material for Western blot analysis (Figure 5–figure
237 supplement 2). Thus, individual Munc13 isoforms appear to show inherent
238 differences in their ability to promote LDCV release in chromaffin cells.

239

240 **LDCV docking in the absence of ubMunc13-2 and Munc13-1**

241 We went on to investigate whether *Unc13a*^{KO}*Unc13b*^{KO} chromaffin cells show an
242 LDCV docking defect analogous to the SV docking defect seen in

243 *Unc13a*^{KO}*Unc13b*^{KO} synapses (Siksou et al., 2009). SV docking deficits of
244 Munc13/Unc-13 deficient synapses in mice and *C. elegans* were previously only
245 detected when rapid cryo-fixation methods were employed instead of classical
246 chemical fixation for ultrastructural analysis (Siksou et al., 2009; Weimer et al.,
247 2006). Moreover, it has been shown that 3D electron tomography (ET) allows a more
248 accurate assessment of SV docking at the active zone (Imig et al., 2014; Siksou et al.,
249 2009). To study LDCV recruitment and docking in chromaffin cells, we therefore
250 combined high-pressure freezing (HPF) and freeze-substitution of acute adrenal gland
251 slices with classical 2D-EM (Figure 6A-E) and high-resolution 3D-ET analyses
252 (Figure 6F-N). Quantitative analysis of 2D-EM images of *Unc13a*^{Het}*Unc13b*^{Het}
253 (Figure 6A) and *Unc13a*^{KO}*Unc13b*^{KO} chromaffin cells (Figure 6B) did not reveal any
254 differences in LDCV distribution within 2 μm of the plasma membrane (PM) (Figure
255 6C), in the number of membrane-proximal LDCVs within 40 nm of the PM (Figure
256 6D), or in the total number of LDCVs (Figure 6E). LDCV docking and recruitment
257 into the vicinity of the PM were assessed using 3D-ET (Figure 6F-N). From all
258 LDCVs analyzed within 100 nm of the PM, the percentage of membrane-proximal
259 LDCVs (0-40 nm) (Figure 6M) and their distribution (Figure 6L) was unaltered
260 between both groups, indicating that LDCV recruitment to the PM is intact in
261 Munc13-deficient chromaffin cells. The number of docked LDCVs, defined as
262 LDCVs in physical contact with the PM and assigned to the 0-4 nm bin in Figure 6L,
263 and the number of docked LDCVs normalized to the number of membrane-proximal
264 LDCVs (Figure 6N) were unchanged. Furthermore, the average LDCV diameter of
265 docked or non-docked LDCVs, measured by 3D-ET, did not differ significantly
266 between genotypes, although *Unc13a*^{KO}*Unc13b*^{KO} LDCVs tended to be smaller
267 (Figure 6–figure supplement 1). Thus, in spite of the dramatic release deficit seen in

268 *Unc13a*^{KO}*Unc13b*^{KO} chromaffin cells and the dramatic SV docking deficit seen in
269 neurons of this genotype (Siksou et al., 2009), we did not detect any changes in
270 LDCV docking, nor a loss or accumulation of LDCVs in the vicinity of the PM. Thus,
271 chromaffin cells can generate what appears to be a full-sized pool of morphologically
272 docked LDCVs in the absence of Munc13-1 and Munc13-2, which implies that the
273 molecular requirements of morphological LDCV and SV docking are distinct.
274 Additionally, this could either indicate that the mechanism of functional docking, i.e.
275 priming, differs between LDCV and SVs as well, or else, that the primed LDCVs (i.e.
276 those that belong to the RRP) are in the minority among the docked vesicles and
277 therefore cannot be detected.

278 To distinguish between these two possibilities, we estimated the total number of
279 docked LDCVs per cell. To this end, we re-calculated the percentage of docked
280 vesicles identified using 3D-ET, as the percentage of membrane proximal vesicles (0-
281 40 nm) identified in the 2D-EM analysis and converted LDCVs/ μ m PM to
282 LDCVs/cell as described (Parsons et al., 1995). This conversion was necessary due to
283 the limited volume sizes analyzed by 3D-ET and the uneven distribution of LDCVs
284 within the cells. The estimated size of the morphologically docked pool was ~662
285 LDCVs per chromaffin cell in control cells. For *Unc13a*^{KO}*Unc13b*^{KO} cells we
286 calculated ~865 docked LDCVs per cell, which can be accounted for by two factors
287 used in the calculation: *Unc13a*^{KO}*Unc13b*^{KO} cells are slightly larger, and their LDCVs
288 are slightly smaller (Figure 6–figure supplement 1). Both values are lower than the
289 previously reported ~1607 for embryonic day (E)18 murine chromaffin cells (de Wit,
290 2010), presumably reflecting improved discrimination between docked and undocked
291 vesicles by 3D-ET. With a diameter of a docked LDCV of ~170 nm (Figure 6–figure
292 supplement 1E) and assuming a specific membrane capacitance of 1 μ F/cm², this

293 corresponds to a vesicular capacitance of 0.91 fF, in excellent agreement with recent
294 electrophysiological measurements of 0.94 fF (Pinheiro et al., 2014). Thereby, the
295 size of the RRP, which is <40 fF at resting $[Ca^{2+}]$ (Voets, 2000), corresponds to <44
296 vesicles from the total of ~662 in control cells, indicating that even with 3D-ET, the
297 RRP will be very hard or even impossible to distinguish morphologically from other
298 docked vesicles in adrenal chromaffin cells.

299

300 **Identification of a Munc13-sensitive step in LDCV priming**

301 Thus far, our data indicate that although morphological docking of LDCVs does not
302 require Munc13s, the priming of a functional RRP does. We therefore wanted to
303 identify the Munc13-sensitive step in the LDCV priming process, and compare the
304 intrinsic properties of Munc13-1 and ubMunc13-2, the two most relevant isoforms in
305 the adrenal medulla. In a recently published mathematical model for LDCV fusion,
306 we showed that the fast and slow bursts of release originate from two serially
307 arranged pools of vesicles, the RRP and the non-releasable NRP, respectively (Walter
308 et al., 2013) (Figure 7). The NRP in turn is refilled from a larger depot pool. Thus, the
309 model features two separate priming steps (Liu et al., 2010), but only one fusion
310 pathway (Figure 7E). Since the deletion of *Unc13a* and *Unc13b* changed the fast and
311 slow burst to nearly the same degree (Figure 2F), within the framework of this model,
312 Munc13s must act upstream of the NRP. Furthermore, since the sustained release rate
313 is changed proportionally as well, Munc13s likely act to accelerate the forward
314 priming rate, k_1 (Ashery et al., 2000). In most models, this rate constant k_1 is Ca^{2+} -
315 dependent (Voets, 2000; Walter et al., 2013), and confers overall Ca^{2+} -dependence to

316 the primed vesicle pool. We next investigated how the two relevant Munc13-isoforms
317 in chromaffin cells (ubMunc13-2, Munc13-1) affect this priming step.

318 The Ca^{2+} -dependence of LDCV-priming (essentially k_1 in Figure 7E) can be assessed
319 in an experiment by varying the pre-flash intracellular $[\text{Ca}^{2+}]$, before an uncaging
320 flash is used to probe the size of the primed vesicle pool (Voets, 2000). We expressed
321 either Munc13-1 or ubMunc13-2 in *Unc13a*^{KO}*Unc13b*^{KO} cells and extended the range
322 of pre-flash $[\text{Ca}^{2+}]$ values from the previously used 300-600 nM (Figure 2 and Figure
323 5) to 250-1200 nM (Figure 7A and Figure 7-figure supplement 1). In order to
324 compare the respective Ca^{2+} -sensitivities rather than the absolute priming rates of
325 Munc13-1 and ubMunc13-2 – and to overcome cell-to-cell variability – we
326 normalized capacitance traces to their value after 3 s (Figure 7A, left and middle
327 panels). Using the fractional increase in capacitance after 30 ms as a read-out of the
328 primed vesicle pool, we identified the characteristic Ca^{2+} -dependence of priming.
329 Strikingly, the Ca^{2+} -dependence was almost identical for the two isoforms and could
330 be fitted with a single Hill equation (Figure 7A right-hand panel, Table 1).

331 Thus, Ca^{2+} -dependent priming is supported with identical steady-state affinities in the
332 presence of Munc13-1 or ubMunc13-2. However, when applying Ca^{2+} -uncaging
333 flashes from a relatively low pre-flash $[\text{Ca}^{2+}]$, the two isoforms induce quite different
334 secretion kinetics (Figure 7B,C). For ubMunc13-2, secretion shows a clear sigmoid
335 shape with acceleration after ~0.5 s (Figure 7C), which is absent when the pre-flash
336 $[\text{Ca}^{2+}]$ is higher. This sigmoid shape of ubMunc13-2 driven secretion was noted
337 before and was attributed to a slow association of ubMunc13-2 with Calmodulin and
338 Ca^{2+} , resulting in a slow “priming switch” (Zikich et al., 2008). In contrast, Munc13-1
339 does not show this secondary acceleration (Figure 7B), regardless of the pre-flash
340 $[\text{Ca}^{2+}]$. To understand the origin of this behavior, we modeled the Ca^{2+} association

341 with the priming sensor (PS) explicitly - in our previous model (Walter et al., 2013),
342 this step had been assumed to be always in equilibrium. In accordance with the
343 observed identical steady state Ca^{2+} dependencies (Figure 7A), we used identical
344 dissociation constant (K_D) values for both isoforms, and varied only the on-rate, k_{on} ,
345 (the off-rate was changed simultaneously, $k_{\text{off}} = K_D * k_{\text{on}}$, with constant K_D). This led
346 to a very satisfactory fit to both Munc13-1 and ubMunc13-2 data from both low and
347 high pre-flash $[\text{Ca}^{2+}]$ (Figure 7B,C). Also, this model made it possible to fit both the
348 control trace, and the *Unc13b*^{KO} trace (Figure 7D). Importantly, the fit was performed
349 simultaneously to all traces, so that we could ensure consistency between fits,
350 simplify the interpretation of parameter changes, and ensure that all conditions could
351 be reproduced by one version of our model (for fitted parameters, refer to Table 1).

352 Our model (Figure 7E) assumes that the NRP vesicles can only fuse after maturing to
353 the RRP state (Walter et al., 2013). Earlier models assumed that the 'NRP pool' can
354 fuse directly via an alternative pathway; in those cases, the corresponding pool was
355 called 'Slowly Releasable' (SRP) (Voets, 2000). We note that our conclusion that
356 Munc13-1/ubMunc13-2 exert their main effects upstream of both pools (NRP/SRP
357 and RRP), i.e. on k_1 , is consistent with both ideas (see also Ashery et al., 2000).
358 Therefore our observations here do not necessarily distinguish between the parallel
359 pool model (SRP and RRP are both releasable) and the sequential pool model (only
360 the RRP is releasable); but see (Walter et al., 2013) for data supporting the sequential
361 pool model).

362 The modeling resulted in two main conclusions (Table 1): First, as expected, the
363 action of Munc13 (either isoform) is consistent with an increase in k_1 – the forward
364 rate of priming within the first priming step (Figure 7E). This is seen both by the
365 increase in the fitted k_1 upon overexpression of either isoform, and by the decrease of

366 k_1 in the *Unc13b*^{KO} cells. Second, ubMunc13-2 increases k_1 4.5-fold more than
367 Munc13-1, but it does so after a longer delay. In the model, this delay is due to slower
368 kinetics of Ca^{2+} binding to the priming sensor (Zikich et al., 2008). Note that this step
369 might coincide with the translocation of Munc13-1 or ubMunc13-2 to the membrane
370 as a prerequisite for the priming action of the protein. Thus, the different delays might
371 reflect differences in the membrane translocation step. As a minor note, we also
372 noticed that k_2 , the forward rate of downstream priming (“priming 2”, Figure 7E)
373 always changed in the opposite direction of k_1 . The reason for this is unclear, but one
374 explanation could be that the protein(s) driving downstream priming compete with
375 Munc13 for association with the fusion machinery.

376

377

378 **Discussion**

379 Our study provides a comprehensive analysis of the Munc13 protein family in LDCV
380 docking and priming, and shows that genetic deletion of Munc13-1 (*Unc13a*) and
381 Munc13-2 (*Unc13b*) severely impairs LDCV release in chromaffin cells. Yet
382 surprisingly, LDCV docking, unlike SV docking, does not require Munc13s. We
383 furthermore identify the step most sensitive to Munc13s in the LDCV priming
384 process, and show that ubMunc13-2 and Munc13-1 accelerate this step with identical
385 Ca^{2+} affinities but distinct Ca^{2+} binding rates.

386 The essential role of Munc13s in vesicular release appears to lie in the opening of
387 Syntaxin (Stx-1)/Munc18-1 complexes, to permit the formation of Stx-1/SNAP-25
388 heterodimers that act as docking platforms for the vesicular SNARE protein
389 Synaptobrevin-2 (Syb-2) (Hammarlund et al., 2007; Ma et al., 2011; Ma et al., 2013;
390 Richmond et al., 1999; Sassa et al., 1999; Yang et al., 2015). SNARE complex
391 assembly is thought to proceed in an N- to C-terminal zipper-like fashion (Fasshauer
392 and Margittai, 2004; Pobbati et al., 2006; Sorensen et al., 2006; Walter et al., 2010),
393 and, at least for SVs, this assembly seems to be the molecular correlate of both the
394 physical docking process, and acquisition of fusion competence, which is referred to
395 as priming (Imig et al., 2014). However, as will be discussed below, morphological
396 docking of LDCVs does not require Munc13s (Figure 6), yet the priming of a full-
397 sized RRP does (Figure 2), indicating that LDCV docking and functional priming do
398 not represent a one-step process in neuroendocrine cells.

399

400

401 **LDCV and SV docking have distinct requirements**

402 Our data demonstrate that although Munc13s are critical for functional priming of
403 LDCVs in chromaffin cells, morphological LDCV docking, even when assessed by
404 3D-ET at unprecedented resolution, is not impaired in the absence of Munc13s
405 (Figure 6). Thus, in contrast to synapses, where most, if not all docked SVs are part of
406 the RRP, the majority of docked LDCVs in chromaffin cells are not primed, and the
407 functional RRP therefore cannot be distinguished from other docked LDCVs by
408 current ultrastructural methods. Although we cannot completely exclude the
409 possibility that Munc13-3 and Munc13-4 may be present at very low levels, that we
410 were unable to detect (Figure 1), it seems unlikely that their presence could account
411 for the full-sized pool of docked LDCVs in *Unc13a^{KO}Unc13b^{KO}* cells.

412 This raises the question of how the non-primed LDCVs are docked. SV docking
413 requires the SNARE proteins Stx-1, SNAP-25, and Syb-2, as well as Munc13s and
414 CAPSs, but not necessarily the Ca²⁺ sensor of fusion, Synaptotagmin-1 (Syt-1) (Imig
415 et al., 2014). By contrast, current models imply that LDCV docking is mediated by
416 Syt-1, possibly via interaction with the Stx-1/SNAP-25 acceptor complex (de Wit et
417 al., 2006; de Wit et al., 2009; Parisotto et al., 2012). Additionally, Munc18-1 docks
418 LDCVs via its interaction with the closed form of Stx-1 (Gandasi and Barg, 2014;
419 Gerber et al., 2008; Gulyas-Kovacs et al., 2007; Han et al., 2011; Voets et al., 2001)
420 and is also involved in an additional tethering step (Toonen et al., 2006). The
421 vesicular SNAREs seem to be dispensable for docking in chromaffin cells
422 (Borisovska et al., 2005; Gerber et al., 2008), although they have been implicated in
423 PC12 cells (Wu et al., 2012). Some of these discrepancies are most likely due to
424 methodological and terminological differences as well as to limitations in assessing
425 true membrane attachment. However, since we used the same experimental approach

426 previously employed to detect SV docking deficits (Imig et al., 2014; Siksou et al.,
427 2009), our data clearly show that the molecular requirements of SV and LDCV
428 docking are distinct. More specifically, while the formation of the docked/primed
429 RRP requires Munc13s in both cases, and thus appears to be mechanistically quite
430 similar for SVs and LDCVs, the non-primed LDCVs in chromaffin cells appear to
431 dock via a separate, Munc13-independent mechanism.

432

433 Our findings are therefore consistent with the following model of LDCV docking and
434 priming: (i) LDCV docking mediated by Munc18-1/Stx-1, this configuration would
435 be the starting point for Munc13-mediated SNARE complex assembly, i.e. priming
436 (Ma et al., 2011; Ma et al., 2013), and in parallel, (ii) LDCV docking mediated by a
437 second configuration, that would not be expected to progress to SNARE complex
438 assembly directly or as efficiently, and thus be consistent with the large unprimed, but
439 docked LDCV pool. What this second configuration would look like in terms of
440 molecular interactions is less clear. Docking via Syt-1/Stx-1/SNAP-25 complexes
441 would be consistent with un-primed docking (de Wit et al., 2009). This mode of
442 docking would require the assumption that in chromaffin cells, Stx-1/SNAP-25
443 complexes can escape NSF/SNAP mediated disassembly. An additional or alternative
444 mode of un-primed docking may involve the recruitment of vesicles based on the
445 interaction of Syt-1 with phosphatidylinositol 4,5-bisphosphate (PIP₂)/Stx-1 clusters
446 (Honigsmann et al., 2013; Park et al., 2015), although further interactions may be
447 required to achieve close membrane apposition.

448 In the model suggested above, we explicitly included only molecular components for
449 which docking deficits have been demonstrated in chromaffin cells. However, LDCV

450 docking most likely involves additional factors. For instance, the docking of LDCVs
451 to Munc18-1/Stx-1 complexes probably requires the interaction between Munc18 and
452 the vesicle-associated small GTPases Rab3 and Rab27 (Graham et al., 2008; Tsuboi
453 and Fukuda, 2006; van Weering et al., 2007), and additional docking/tethering factors
454 may be involved in docking both primed and un-primed LDCVs to the membrane.

455

456 **Release kinetics of LDCV pools as correlates of SNARE complex assembly**

457 Our analysis of how Munc13s prime LDCVs for fusion identifies the earliest phase of
458 the priming process as the step most sensitive to Munc13s. We interpret our data
459 according to a model that features Munc13 as a Ca^{2+} -sensitive priming protein in a
460 single pathway to LDCV fusion with two serially arranged vesicle states or pools
461 (NRP and RRP) (Figure 7E). This essentially allows us to describe what was
462 previously interpreted as the release of two kinetically distinct LDCV pools (SRP and
463 RRP), as two sequential priming processes, priming 1 and priming 2, resulting in only
464 one releasable pool, the RRP (Walter et al., 2013). According to previous data, the
465 step most sensitive to Munc13s – priming 1 – is also the step affected by mutations
466 designed to interfere with the initiation of N-terminal SNARE complex assembly
467 (Walter et al., 2013; Walter et al., 2010). This is in line with a function of Munc13s in
468 initiating SNARE-complex assembly (Yang et al., 2015). The second priming step
469 may involve a downstream, presumably more C-terminal phase of SNARE-complex
470 assembly, although other options remain open. Thus, in the model (Figure 7E), the
471 formation of the NRP, i.e. the step most sensitive to Munc13s, most likely represents
472 the initiation of N-terminal SNARE complex assembly.

473

474 **Catalysis of fast and slow LDCV priming by Munc13-1 and ubMunc13-2**

475 As our study demonstrates, Munc13 isoforms differ in their ability to facilitate LDCV
476 priming (Figure 5). We detected three endogenously expressed isoforms in murine
477 chromaffin cells, Munc13-1, ubMunc13-2, and Baiap3 (Figure 1). Baiap3, somewhat
478 surprisingly given its prominent expression and ability to translocate to membranes in
479 a Ca^{2+} -dependent manner (Lecat et al., 2015), does not appear to be involved in
480 LDCV priming in this cell type. However, Munc13-4, which regulates SNARE-
481 mediated vesicle exocytosis in the hematopoietic system (Boswell et al., 2012;
482 Feldmann et al., 2003; Shirakawa et al., 2004), and is the closest relative of Baiap3
483 (Koch et al., 2000), can promote LDCV priming, albeit less efficiently than Munc13-
484 1 and ubMunc13-2.

485 The two most relevant isoforms, Munc13-1 and ubMunc13-2, promote LDCV
486 priming with very similar steady-state Ca^{2+} -affinities, but nonetheless confer unique
487 release kinetics depending on the pre-stimulus $[\text{Ca}^{2+}]$. Modeling of the secretion
488 kinetics produced by overexpression of Munc13-1 and ubMunc13-2 in
489 *Unc13a^{KO}Unc13b^{KO}* cells allowed us to isolate the intrinsic properties of each isoform
490 (Table 1). Secretion driven solely by the dominant isoform ubMunc13-2 shows a
491 characteristic sigmoid shape at low pre-stimulus $[\text{Ca}^{2+}]$ (Figure 7C) (Zikich et al.,
492 2008). In our secretion model, the best-fit parameters indicate 2.5-fold slower sensing
493 of $[\text{Ca}^{2+}]$ for ubMunc13-2, which can however accelerate priming dramatically when
494 $[\text{Ca}^{2+}]$ increases. Thus, the fitted maximum priming rate (k_1) for ubMunc13-2 is 4.5-
495 fold higher than for Munc13-1. However, although Munc13-1 is unable to support the
496 same maximum priming rate as ubMunc13-2, it reacts faster to a change in the $[\text{Ca}^{2+}]$
497 concentration (Figure 7B), which may reflect distinct conformational changes in
498 response to $[\text{Ca}^{2+}]$, and/or differences in a membrane translocation step.

499

500 Thus, neuroendocrine cells can fundamentally modify the kinetics of secretion by
501 expressing different Munc13 isoforms. Previous data from autaptic neurons showed
502 that Munc13-1 causes short term depression, whereas ubMunc13-2 causes short-term
503 facilitation (Rosenmund et al., 2002), which parallels our findings in chromaffin cells
504 from low basal $[Ca^{2+}]$, raising the possibility that the functions of different Munc13
505 isoforms in priming LDCVs and SVs are conserved, even though their role in docking
506 is not. Our model therefore provides a theoretical framework for how the molecular
507 properties of priming factors may be linked to the kinetics of exocytosis.

508

509 **Sequential actions of upstream and downstream priming catalysts**

510 Although Munc13s have the strongest effect on the priming step 1, i.e. the formation
511 of the NRP vesicle state, they also influence priming step 2, i.e. the formation of the
512 RRP. Remarkably, overexpression and deletion of Munc13s change the rate constants
513 k_1 (priming 1) and k_2 (priming 2) in opposite directions (Figure 7D). One possible
514 reason for this effect could be that the interaction of Munc13s with the SNARE fusion
515 machinery may compete with that of another priming protein, which mainly catalyzes
516 priming step 2. A likely candidate for this second catalyst appears to be CAPS, as
517 deletion of CAPS1 and CAPS2 leads to a significant reduction of the RRP, but has
518 little effect on the NRP/SRP, placing Munc13 upstream of CAPS (Liu et al., 2010;
519 Liu et al., 2008).

520 Furthermore, in PC12 cells, strong stimulation bypasses the need for CAPS-1 in
521 LDCV exocytosis, but not the need for ubMunc13-2 (Kabachinski et al., 2014), and

522 the ability of CAPS to promote membrane fusion is impaired by C-terminal mutations
523 in Stx-1 (Daily et al., 2010). We therefore propose an LDCV priming model, in which
524 the Munc13-driven priming step 1 corresponds to the initiation of N-terminal
525 SNARE-complex assembly, and the CAPS-driven priming step 2 represents a more
526 C-terminal, and presumably more easily completed phase of zippering (Gao et al.,
527 2012). Assuming that priming step 2 is not catalyzed by CAPS alone but also
528 influenced by Munc13 and possibly Syt-1, such a model would also offer an
529 explanation as to why in both SV and LDCV exocytosis, lack of CAPS can be
530 compensated for by an increase in Ca^{2+} , whereas lack of Munc13 cannot (Jockusch et
531 al., 2007; Kabachinski et al., 2014).

532

533 **Conclusion**

534 In summary, our data show that mammalian neurons and neuroendocrine cells both
535 require Munc13s to generate fusion-competent vesicles, although the molecular steps
536 leading to LDCV docking prior to SNARE complex assembly appear to be unique. In
537 LDCV priming, the step most sensitive to Munc13s is the initial phase (priming step
538 1), which most likely corresponds to the initiation of N-terminal SNARE-complex
539 assembly. Individual Munc13 isoforms accelerate this step at distinct rates, thereby
540 imparting distinct properties on the kinetics of LDCV release, which indicates that
541 they may have specialized functions in the fine-tuning of catecholamine release in
542 response to varying physiological stimuli.

543

544 **Materials and methods**

545 **Animals**

546 All experiments were performed in compliance with the regulations of the local
547 Animal Care and Use Committee of Lower Saxony, Oldenburg, Germany. The
548 generation and basic characterization of the KO lines of the Munc13 isoforms has
549 been described previously (Augustin et al., 2001; Augustin et al., 1999; Varoqueaux
550 et al., 2002; Wojcik et al., 2013). *Unc13d*^{KO} (*Unc13d*^{lox}) mice (Croizat et al., 2007)
551 were obtained from Jackson Laboratories. Adult and perinatal mice were killed by
552 decapitation prior to the removal of adrenal glands and other tissues.

553

554 **Western blotting and antibodies**

555 Adrenal glands of perinatal animals were excised and stored at -80°C prior to use.
556 Adrenal glands from around 20 perinatal animals were pooled for the preparation of
557 homogenates. Homogenates of whole adrenal glands were prepared by
558 homogenization in an ice-cold buffer (320 mM D-glucose, 20 mM HEPES, 2 mM
559 EDTA, pH 7.4, with 0.5 µg/ml leupeptin, 1 µg/ml aprotinin and 0.1 mM PMSF added
560 freshly prior to homogenization), using a Potter S homogenizer. For the preparation of
561 adrenal cortical and medullary homogenates, adrenal glands from WT animals were
562 dissected in ice-cold buffer containing 19 mM NaH₂PO₄ and 81 mM Na₂HPO₄ and
563 material from 5-6 animals was pooled. Spleen homogenates were prepared similarly
564 and the DNA in the samples subsequently digested with 0.66 U/µl benzonase (E1014,
565 Sigma-Aldrich) in 3.86 mM MgCl₂ for 10 min at 37°C prior to denaturation. Whole
566 brain homogenates were prepared using a Potter S homogenizer and centrifuged for

567 10 min at 1000 g at 4°C to remove the nuclear fraction. Homogenates were analyzed
568 by Western blotting with the following antibodies at the indicated dilutions: rabbit-
569 anti-Munc13-1 (1:500) (126103, Synaptic Systems), rabbit-anti-ubMunc13-2
570 (1:2000), rabbit-anti-bMunc13-2 (1:1000), rabbit-anti-Munc13-3 (1:500)
571 (Varoqueaux et al., 2005), rabbit-anti-Baiap3 (1:1000) (Wojcik et al., 2013), goat-
572 anti-Munc13-4 (1:250) (NB100-41385; Novus Biologicals), rabbit-anti-
573 Chromogranin A (1:8000) (259002; Synaptic Systems), mouse-anti-GFP (1:500)
574 (11814460001; Roche), mouse-anti-valorin containing protein (VCP) (1:1000)
575 (612182; BD Transduction Laboratories), and mouse-anti-GAPDH (1:25000)
576 (ab8245; Abcam). Secondary antibodies (goat anti-rabbit IgG, 111035144; goat anti-
577 mouse IgG, 115035146, donkey anti-goat, 705-035-147) were obtained from Jackson
578 ImmunoResearch.

579

580 **Chromaffin cell culture**

581 Chromaffin cell cultures were prepared as described in Sørensen et al. (Sorensen et
582 al., 2003b). Cultures from *Unc13a*^{KO} and *Unc13a*^{KO}*Unc13b*^{KO} mice were prepared on
583 embryonic day (E)18, and from *Unc13b*^{KO}, *Unc13c*^{KO}, and *Baiap3*^{KO} mice on
584 postnatal day (P)0, in each case using littermates of the appropriate genotypes as
585 controls. For overexpression of Baiap3 in WT cells, chromaffin cells from P0 WT
586 C57Bl/6N mice were used. Briefly, adrenal glands were excised and placed into ice-
587 cold Locke's solution (154 mM NaCl, 5.6 mM KCl, 0.84 mM NaH₂PO₄, 2.14 mM
588 Na₂HPO₄ and 10 mM D-glucose, pH 7.0). The glands were then transferred to 300 µl
589 of a papain solution [20 U/ml papain (Worthington Biochemical), 200 mg/L L-
590 cysteine, 1 mM CaCl₂, 0.5 mM EDTA, in DMEM (Gibco)], which had been

591 equilibrated for 15 min with 95 % O₂ and 5 % CO₂, and incubated with gentle shaking
592 for 45 min at 37°C. To terminate the papain digestion, 300 µl of inactivating solution
593 [10 % fetal bovine serum (Gibco), 2.5 g/L trypsin inhibitor (Gibco) and 2.5 g/L
594 albumin in DMEM (Gibco)] were then added, followed by an incubation period of 5
595 min at 37°C. The mixture of solutions was then replaced by 160 µl of DMEM
596 (Linaris) supplemented with 1 % insulin-transferrin-selenium X (Gibco) and 200 U/L
597 penicillin-streptomycin (Gibco). The glands were triturated with a 200-µl pipette tip
598 and the cell suspension was placed as 50 µl drops on coverslips in a 6-well plate.
599 Following an incubation period of 30 min at 37°C at 8 % CO₂ to allow cells to settle,
600 2 ml of DMEM (Linaris) with the supplements described above were added per well
601 and the cells were kept at 37°C and 8 % CO₂. The cells were used for
602 electrophysiological recordings on days *in vitro* 2-3.

603

604 **Viral constructs**

605 Expression constructs based on the SFV plasmid (pSFV1) for Munc13-1 and
606 ubMunc13-2, both subcloned in frame with a C-terminal EGFP, have been described
607 previously (Rosenmund et al., 2002). Munc13-4 and Baiap3 pSFV1 expression
608 constructs were generated as IRES-EGFP constructs using the full-length mouse
609 cDNAs. Production of SFV particles was done according to published protocols
610 (Ashery et al., 1999). Briefly, pSFV1 constructs and pSFV-helper2 DNA were
611 linearized with Spe I and transcribed into RNA using SP6 RNA polymerase. RNA
612 from the pSFV1 constructs and the pSFV-helper2 construct, 10 µg each, were
613 electroporated (500 V, 0.957 mF) into baby hamster kidney 21 cells. Supernatant of
614 cell cultures containing the virus was collected after 24 h. In cases where the virus

615 titer was low, the supernatant was concentrated approximately 25-fold using a filter
616 unit with a nominal molecular weight limit of 100 kDa (UFC910024, AMICON).
617 SFV particles encoding the respective Munc13 isoforms with EGFP or only EGFP as
618 a control were added to chromaffin cell cultures, infected cells identified based on the
619 EGFP fluorescence, and electrophysiological recordings performed 4-6 h after
620 addition of the virus.

621

622 **Whole-cell capacitance measurements**

623 Whole cell patch-clamping was performed with Sylgard-coated 4-6 M Ω pipettes
624 (Science Products) at a setup equipped with a Zeiss Axiovert 200 microscope (Zeiss)
625 and a HEKA EPC-10 amplifier controlled by Patchmaster (HEKA). Capacitance
626 measurements were performed according to the Lindau-Neher technique using the
627 „sine+dc“ mode in the Lockin Extension of Patchmaster. The frequency and peak-to-
628 peak amplitude of the sine wave were 1042 Hz and 70 mV, respectively, and the
629 holding potential was -70 mV. Recordings were sampled at 12.5 kHz and filtered at
630 2.9 kHz. Flash photolysis experiments were performed according to established
631 protocols (Voets, 2000; Walter et al., 2010). The extracellular solution contained 147
632 mM NaCl, 10 mM HEPES, 11.1 mM D-glucose, 2.8 mM KCl, 2 mM CaCl₂, 1 mM
633 MgCl₂ and 3 μ M tetrodotoxin (pH 7.2, 300-310 mOsM). For flash experiments, the
634 intracellular solution contained 109 mM L-glutamic acid, 35 mM HEPES, 5 mM
635 nitrophenyl-EGTA (Synaptic Systems), 5.65 mM CaCl₂, 2 mM Mg-ATP, 0.3 mM
636 Na-GTP, 0.205 mM fura-4F (Invitrogen), 0.3 mM furaptura (Invitrogen) and 1 mM
637 ascorbic acid (titrated to pH 7.2 with CsOH, osmolarity 290-295 mOsM). The flash
638 stimulus was applied approximately 80 s after the whole-cell configuration was

639 established using a xenon lamp (Rapp OptoElectronics). Unless otherwise specified,
640 only cells with pre-flash $[Ca^{2+}]$ in the range of 300-600 nM were used for analysis. In
641 flash photolysis experiments requiring pre-flash $[Ca^{2+}]$ concentrations higher than 600
642 nM (Figure 7 and Figure 7-figure supplement 1), pulses of light at wavelengths of
643 340 and 380 nm were applied at varying frequencies to release Ca^{2+} from nitrophenyl-
644 EGTA and the cell was kept at the target $[Ca^{2+}]$ for ~20 s before the flash stimulus
645 was given. The pre-flash $[Ca^{2+}]$ was taken as the averaged measured $[Ca^{2+}]$ during the
646 20 s period. In depolarization experiments, the same extracellular solution was used
647 except that tetrodotoxin was omitted. The intracellular solution contained 111 mM L-
648 glutamic acid, 35.5 mM HEPES, 17 mM NaCl, 1 mM $MgCl_2$, 2 mM Mg-ATP, 0.3
649 mM Na-GTP (titrated to pH 7.2 with CsOH, osmolarity 290-295 mOsM), and fura-4F
650 and furaptra at the same concentration used in flash experiments. In flash photolysis
651 experiments, pool sizes (fast and slow bursts) and their time constants were obtained
652 by fitting a sum of exponential functions to the capacitance traces (Sorensen et al.,
653 2003b), using a custom macro (Three-Exponential-Fit-Macro-Igor) with the software
654 IgorPro (WaveMetrics). The near-linear rate of release of the sustained component is
655 measured as a linear component with the unit capacitance increase per second. The
656 exocytotic delay was defined as the time point where the exponential fit meets the
657 pre-flash capacitance.

658

659 **Ca^{2+} measurements**

660 In flash experiments, exocytosis was stimulated by a sudden elevation of intracellular
661 $[Ca^{2+}]$ using UV flash stimuli given by a xenon flash lamp (Rapp OptoElectronics).
662 $[Ca^{2+}]$ measurements were performed according to established protocols (Voets,

663 2000; Walter et al., 2010). The ratiometric Ca^{2+} indicator dyes fura-4F and furaptra
664 were alternately excited at 340 and 380 nm using a Polychrome V monochromator
665 (TILL Photonics), and the emitted light was detected with a photomultiplier. The area
666 of fluorescence measurement was limited to the diameter of the cell. The 340/380 nm
667 fluorescence ratio was independently calibrated at the same dye concentrations with a
668 range of intracellular solutions with known $[\text{Ca}^{2+}]$, buffered with Ca^{2+} buffers 1,2-
669 bis(o-aminophenoxy)ethane-N,N,N',N'-tetraacetic acid (BAPTA, Invitrogen) and
670 diethylenetriaminepentaacetic acid (DPTA, Sigma-Aldrich). The $[\text{Ca}^{2+}]$ of the
671 calibration solutions was calculated using K_D of BAPTA = 0.222 μM and K_D of
672 DPTA = 80 μM .

673

674 **Amperometry**

675 Amperometric recordings were performed using carbon fibers of 5 μm diameter
676 (Thornel P-650/42; Cytec, NJ, USA), insulated using the polyethylene method
677 (Bruns, 2004). Vesicle fusion was triggered by infusing the cells through the patch
678 pipette with a solution containing 4.6 μM free Ca^{2+} . The fibers were clamped at 700
679 mV and currents were hardware filtered at 3 kHz using an EPC-7 patch clamp
680 amplifier (HEKA). Currents were digitized at 25 kHz and filtered off-line using a
681 Gaussian filter with a cut-off set at 1 kHz. Filtering, spike detection, and analysis
682 were performed using a freely available, custom-written macro (Mosharov and
683 Sulzer, 2005) running under IgorPro (Wavemetrics, Lake Oswego, OR). A spike
684 detection threshold of 5 pA and a foot detection threshold of 2 pA were imposed. For
685 each analyzed cell, the median of each parameter (duration, halftime, amplitude,
686 charge, rise time, decay time, foot amplitude, foot duration, foot charge) was

687 calculated from all spikes, and this value was used for averaging between cells
688 (giving the mean of cell medians).

689

690 **High-pressure freezing of adrenal gland slices for EM analysis**

691 Adrenal glands from E18 animals were embedded in 3% low gelling agarose (Sigma-
692 Aldrich) and adrenal gland slices were prepared according to published protocols
693 (Moser and Neher, 1997). Slices were allowed to recover in bicarbonate-buffered
694 saline (125 mM NaCl, 26 mM NaHCO₃, 2.5 mM KCl, 1.25 mM NaH₂PO₄, 2 mM
695 CaCl₂, 1 mM MgCl₂, 10 mM D-glucose and 0.2 mM (+)-tubocurarine) at 37°C for 15
696 min and were subsequently kept in the same solution at RT before cryofixation. Slices
697 were rapidly frozen in external cryoprotectant (20% BSA in bicarbonate-buffered
698 saline) using a HPM100 HPF device (Leica). After freezing, samples were stored in
699 liquid nitrogen until further processing. Freeze substitution was performed as
700 previously published (Rostaing et al., 2006). Briefly, samples were substituted in
701 anhydrous acetone, fixed by 2% OsO₄ in acetone for 7h at -90°C prior to a
702 temperature ramp (5°C/h) to -20°C, an incubation for 16 h at -20°C, and a final ramp
703 (10°C/h) to 4°C. Samples were washed in acetone and infiltrated with EPON resin at
704 room temperature (acetone/EPON 1:1 for 3 h, 90% EPON in acetone overnight, and
705 pure EPON for 36 h). Finally specimen carriers containing infiltrated samples were
706 incubated for 24 h at 60°C to polymerize. Aluminum sample carriers were trimmed
707 off the EPON block with a specimen trimming device (EM TRIM2, Leica) to expose
708 the surface of the embedded tissue for ultramicrotomy.

709

710 **Sectioning, contrasting, and fiducial marker application for EM**

711 An Ultracut UCT ultramicrotome (Leica) was used to cut 500 nm-thick sections until
712 the first tissue appeared. Ultrathin (50 nm) and semithin (400 nm) sections were then
713 collected onto Formvar-filmed, carbon-coated copper slot or mesh grids for 2D and
714 3D ultrastructural analysis, respectively. Vitrified samples were subjected to rigorous
715 quality control (Mobius et al., 2010) and samples exhibiting indications of ice-crystal
716 damage were excluded from the analysis. Ultrathin sections were post-stained with
717 1% uranyl acetate in ddH₂O for 30 min, washed several times in ddH₂O, stained with
718 0.3% lead citrate for 2 min, washed, and dried with filter paper. For 3D-tomographic
719 analysis, 400 nm-thick sections were briefly incubated in a solution of Protein A
720 conjugated to 10 nm gold particles (Cell Microscopy Center, Utrecht, The
721 Netherlands) to introduce fiducial markers.

722

723 **2D-EM analysis of chromaffin cells**

724 Electron micrographs (2048 x 2048 pixels) were acquired with a sharp:eye CCD
725 camera (Tröndle, TRS) at 5,000 fold magnification using the multiple image
726 acquisition and alignment feature of iTEM software (version 5.1, Olympus Soft
727 Imaging Solutions GmbH). Assembled montages had dimensions of approximately 21
728 x 21 μm and typically contained 1-3 randomly chosen chromaffin cells. Only
729 chromaffin cells with a clearly visible plasma membrane were included in the
730 analysis. iTEM software was used to measure chromaffin cell plasma membrane
731 circumference and the cytoplasmic area (calculated by subtraction of the nuclear area
732 from the total cell area). Additional parameters including the number of LDCVs and
733 the shortest distance of each LDCV to the plasma membrane were quantified using

734 ImageJ software. In regions where the plasma membrane did not appear as a clear cut,
735 the shortest distance from the vesicle membrane to the middle of the membrane
736 projection was measured. For this reason and due to the fact that LDCVs (mean
737 diameter of CTRL LDCVs ~ 160 nm; ~ 170 nm for docked CTRL LDCVs) might
738 have their centers outside of the imaged ultrathin (50 nm) section, we did not quantify
739 LDCV docking as defined by physical membrane-attachment in these 2D projection
740 images, but rather calculated the number of membrane-proximal LDCVs (within 0-40
741 nm of the plasma membrane). All vesicles with electron-dense cargo were included in
742 the analysis. Secretory vesicles of both genotypes exhibited heterogeneity in size (see
743 Figure 6–figure supplement 1) and appearance (e.g. compactness of the dense-core),
744 possibly reflecting distinct LDCV types (e.g. adrenaline vs. noradrenaline) or
745 different levels of maturity present in immature (E18) chromaffin cells. Data are
746 presented as LDCV density (number of LDCVs per μm^2 area cytoplasm), the number
747 of LDCVs within 40 nm of the plasma membrane normalized to the cell perimeter,
748 and the mean frequency distribution of LDCVs from the plasma membrane in 40 nm
749 bins.

750

751 **3D-EM analysis of LDCV docking in chromaffin cells**

752 For high-resolution electron tomographic analysis of LDCV docking in adrenal
753 chromaffin cells, we randomly selected regions between two neighboring cells that
754 exhibited a high density of LDCVs in proximity of the plasma membrane in thick
755 (400 nm) sections. Single-axis tilt series were acquired from -60° to $+60^\circ$ with 1°
756 increments and binned by the factor two at 10,000 fold magnification using an Orius
757 SC1000 camera (Gatan) and the SerialEM software for automated tilt series

758 acquisition (Mastrorarde, 2005). Tomograms were reconstructed using the IMOD
759 package (Kremer et al., 1996), and exported as z-stacks for analysis with ImageJ
760 (National Institutes of Health). All analyses were performed blindly and manually.
761 The smallest distance between the plasma membrane and the outer leaflet of each
762 LDCV membrane was measured at its vesicular midline using the straight-line tool of
763 ImageJ on individual virtual z-slices. Only vesicles observed in physical contact with
764 the plasma membrane in tomographic volumes were considered ‘docked’. In
765 distribution analyses docked LDCVs were assigned to the 0-4 nm bin to account for
766 the voxel dimensions of reconstructed tomograms (isotropic voxel size = 2.86 nm).
767 The number of membrane-attached (0-4 nm, ‘docked’) LDCVs identified in a
768 tomographically reconstructed volume was normalized to the number of membrane-
769 proximal (0-40 nm of plasma membrane) LDCVs. The number of membrane-
770 proximal (0-40 nm) LDCVs was expressed as a percentage of all LDCVs within 100
771 nm of the plasma membrane and compared across genotypes to test for potential
772 differences in the ability of recruiting LDCVs close to the plasma membrane. The
773 frequency distribution displays the number of docked LDCVs (0-4 nm, first bin) and
774 subsequently the distances of LDCVs from the plasma membrane in 2 nm bins.
775 Statistical analyses were performed using Student’s *t*-test. The mean LDCV diameter
776 was calculated from the area of the LDCV measured at its midline including the
777 vesicular phospholipid bilayer in electron tomograms by using the elliptical selection
778 tool in ImageJ. All LDCVs in the randomly chosen field of view that contained their
779 midline within the tomographic volume were analyzed (Figure 6–figure supplement
780 1).

781

782 For illustrative purposes, figures depicting tomographic subvolumes represent an
783 overlay of 3 consecutive slices produced by the slicer tool of the 3dmod software of
784 the IMOD package to generate a ~ 8.6 nm thick subvolume.

785

786 **Calculation of the number of docked LDCVs per chromaffin cell**

787 The size of the pool of docked LDCVs per cell can be calculated from the number of
788 LDCVs per μm^2 PM area (n_a) (Parsons et al., 1995; Plattner et al., 1997). We
789 measured the number of membrane-proximal LDCVs (0-40 nm of PM) per μm PM
790 length (n_l) in ultrathin sections of 0.05 μm thickness. Our 3D-ET approach permitted
791 us to accurately measure LDCV diameters (d_v in μm) in chromaffin cells (Figure 6–
792 figure supplement 1). The number of LDCVs per μm^2 PM area could then be
793 calculated as $n_a = n_l / (d_v + 0.05)$ (Parsons et al., 1995; Plattner et al., 1997). The
794 average cell surface area (a_c in μm^2) per genotype was estimated based on the average
795 cell capacitance measured in cultured cells assuming 1 $\mu\text{F}/\text{cm}^2$. We chose this
796 method, rather than using the cell circumference measured in ultrathin sections,
797 because the chromaffin cells in adrenal slices are not round, but have rather complex
798 shapes (Figure 6–figure supplement 1). Using either measurement, the
799 *Unc13a*^{KO}*Unc13b*^{KO} cells were slightly larger, by 5% based on capacitance, and by
800 15% based on cell circumference measurements.

801 *Unc13a*^{Het}*Unc13b*^{Het} control cells:

802 n_l : 0.984 ± 0.075 vesicles per μm length

803 d_v : 0.1627 ± 0.005 μm vesicle diameter

804 n_a : 4.627 vesicles per μm^2 PM area

805 a_c : 421.23 μm^2 cell membrane area

806 The estimated number of LDCVs within 40 nm of the PM in *Unc13a*^{Het}*Unc13b*^{Het}
807 chromaffin cells is therefore ~ 1949. Our 3D analysis of LDCV docking revealed that
808 only 33.97% of LDCVs within 40 nm of the PM are physically attached to the PM,
809 therefore we estimated the pool of docked vesicles to contain ~ 662 LDCVs in our
810 acute adrenal slice preparation.

811 *Unc13a*^{KO}*Unc13b*^{KO} cells:

812 n_l : 1.150 ± 0.083 vesicles per μm length

813 d_v : 0.1525 ± 0.003 μm vesicle diameter

814 n_a : 5.679 vesicles per μm² PM area

815 a_c : 442.26 μm² cell membrane area

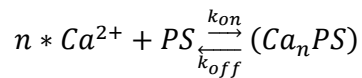
816 The estimated number of LDCVs within 40 nm of the PM in *Unc13a*^{KO}*Unc13b*^{KO}
817 chromaffin cells is therefore ~ 2511. Our 3D analysis of LDCV docking revealed that
818 only 34.43% of LDCVs within 40 nm of the PM are physically attached to the PM,
819 therefore we estimated the pool of docked vesicles to contain ~ 865 LDCVs in our
820 acute adrenal slice preparation.

821

822 **Modeling the Ca²⁺-dependence of vesicle priming**

823 We simulated capacitance traces in Ca²⁺ uncaging experiments with an exocytosis
824 model that was adapted from a previous study of ours (Walter et al., 2013) to
825 explicitly describe the Ca²⁺ dependent vesicle priming reaction. Parameters (Table 1)
826 were either taken from the literature, directly from experiments (Figure 7A), or
827 determined by fitting the model to experimental capacitance traces.

828 We assume that Munc13 proteins act on the Ca^{2+} -dependent priming reaction, which
 829 ensures the refilling of vesicles from a large depot pool (Voets, 2000). We wanted to
 830 explicitly describe this reaction in terms of its thermodynamic steady state binding
 831 properties (i.e. its dissociation constant K_D and cooperativity n), and in terms of its
 832 Ca^{2+} binding kinetics. Let the chemical equation for Ca^{2+} binding to the priming
 833 sensor (PS) be:



834 Then its overall dissociation constant K_D is defined as:

$$835 \quad K_D = \frac{[Ca^{2+}]^n [PS]}{[Ca_n PS]}$$

836 In order to obtain the values of the K_D and n experimentally, we pre-equilibrated
 837 chromaffin cells at different pre-flash $[Ca^{2+}]$ prior to uncaging. The secretion
 838 responses were averaged in bins and normalized to their respective values 3 s after the
 839 flash. Fitting the fraction of release 30 ms after the uncaging stimulus as a function of
 840 pre flash $[Ca^{2+}]$ with the following Hill equation (non-linear curve fitting routine of
 841 Origin Pro 8 G, OriginLab Corporation) allowed us to estimate K_D and n :

$$842 \quad Fraction([Ca^{2+}]) = \frac{[Ca^{2+}]^n}{K_D + [Ca^{2+}]^n} Fmax$$

843 Where $Fraction([Ca^{2+}])$ is the relative release at 30 ms, and $[Ca^{2+}]$ is the pre-flash
 844 Ca^{2+} concentration. $Fmax$, n and K_D are free parameters. The best fit is shown as
 845 solid line in Figure 7 and the values of n and K_D can be found in Table 1.

846 We assume that priming is only increased when the proper number (n) of Ca^{2+} ions
 847 are bound to the PS. Therefore, the rate of priming is proportional to the fraction (f)

848 of PS that has bound the correct number of Ca^{2+} ions divided by the total amount of
 849 PS:

$$f(Ca^{2+}) = \frac{[Ca_nPS]}{[PS_{tot}]}$$

$$k_1(Ca^{2+}) = f(Ca^{2+}) k_{1Max}$$

850 Where k_{1Max} is the asymptotic value of the priming rate for $[Ca^{2+}] \gg K_D$. Since the
 851 total amount of PS is the sum of Ca^{2+} -free and Ca^{2+} -bound PS:

$$f(Ca^{2+}) = \frac{[Ca_nPS]}{[Ca_nPS] + [PS]}$$

852 At steady state, the following relationships hold:

$$f(Ca^{2+})_{SteadyState} = \frac{[Ca^{2+}]^n}{K_D + [Ca^{2+}]^n}$$

$$k_{1SteadyState}(Ca^{2+}) = \frac{[Ca^{2+}]^n}{K_D + [Ca^{2+}]^n} k_{1Max}$$

853 In order to describe temporal changes in this fraction at non-equilibrium conditions,
 854 the Ca^{2+} concentrations ($[Ca^{2+}]$) were interpolated from the experimental values and
 855 the concentration of $[Ca_nPS]$ was calculated at all time points by numerical
 856 integration using the “ode15s” function in Matlab (version R2013a, Mathworks) of
 857 the kinetic equation:

$$\frac{d[Ca_nPS]}{dt} = k_{on}[PS][Ca^{2+}]^n - k_{off}[Ca_nPS]$$

858 We assume that the amount of PS is not limiting (i.e. that each vesicle contains a PS).

859 Then, by investing the relationships

$$[V_{tot}] = [Ca_nPS] + [PS]$$

860 and

$$K_D = \frac{k_{off}}{k_{on}}$$

861 we obtain

$$\frac{d[Ca_nPS]}{dt} = k_{on}([V_{tot}] - [Ca_nPS]) [Ca^{2+}]^n - K_D k_{on} [Ca_nPS]$$

862 Such that the fraction of activated PS can be calculated at time t:

$$f(Ca^{2+}, t) = \frac{[Ca_nPS](t)}{[V_{tot}]}$$

863

864 This allows us to calculate k_1 at all times t.

865

$$k_1(Ca^{2+}, t) = f(Ca^{2+}, t) k_{1Max}$$

866

867 Our model consists of a sequence of mandatory steps for vesicle maturation and
 868 fusion (Walter et al., 2013). Vesicles from the depot enter a non-releasable state
 869 (NRP, Figure 7E) from which they cannot fuse directly. Instead, these vesicles first
 870 need to mature into the readily releasable pool (RRP), a transition that is governed by
 871 a Ca^{2+} -dependent rate constant ($k_2(Ca^{2+})$). This Ca^{2+} -dependence is modeled by a
 872 Ca^{2+} -dependent catalyst as described in Walter et al., 2013:

873

874 $k_2(Ca^{2+})=k_{20}+g(Ca^{2+})k_{2cat}$

875 $k_{-2}(Ca^{2+})=k_{-20}+g(Ca^{2+})k_{-2cat}$

$$k_{-2cat} = \frac{k_{-20}}{k_{20}} k_{2cat}$$

876

877 As in our previous study, we assume that binding of one Ca^{2+} ion activates the

878 catalyst and that the catalyst is in equilibrium with Ca^{2+} , which allows us to calculate

879 $g(Ca^{2+})$:

880

$$g(Ca^{2+}) = \frac{[Ca^{2+}]}{K_{D,cat} + [Ca^{2+}]}$$

881

882 **Kinetic equations of the exocytosis model**

$$\frac{d[Depot]}{dt} = -k_1(Ca^{2+})[Depot] + k_{-1}[NRP]$$

$$\frac{d[NRP]}{dt} = k_1(Ca^{2+})[Depot] - (k_{-1} + k_2(Ca^{2+})) [NRP] + k_{-2}(Ca^{2+})[RRP]$$

$$\frac{d[RRP]}{dt} = k_2(Ca^{2+})[NRP] - (k_{-2}(Ca^{2+}) + 3k_3[Ca^{2+}])[RRP] + k_{-3}[RRPCa]$$

$$\frac{d[RRPCa]}{dt} = 3k_3[Ca^{2+}][RRP] - (k_{-3} + 2k_3[Ca^{2+}])[RRPCa] + 2k_{-3}[RRPCa_2]$$

$$\begin{aligned} \frac{d[RRPCa_2]}{dt} &= 2k_3[Ca^{2+}][RRPCa] - (2k_{-3} + k_3[Ca^{2+}])[RRPCa_2] \\ &\quad + 3k_{-3}[RRPCa_3] \end{aligned}$$

$$\frac{d[RRPCa_3]}{dt} = k_3[Ca^{2+}][RRPCa_2] - (3k_{-3} + k_4)[RRPCa_3]$$

$$\frac{d[F]}{dt} = k_4[RRPCa_3]$$

883

884 **Modeling of exocytosis upon Ca^{2+} uncaging**

885 To find the steady state occupation of the system $k_1(Ca^{2+})$, $k_2(Ca^{2+})$ and
 886 $k_{-2}(Ca^{2+})$ were calculated for the experimental pre-flash Ca^{2+} values, the first five
 887 kinetic equations were taken and set to zero, and mass conservation of vesicles was
 888 obeyed:

$$0 = [Depot]_0 + [NRP]_0 + [RRP]_0 + [RRPCa]_0 + [RRPCa_2]_0 + [RRPCa_3]_0 \\ - [V_{tot}]$$

889 This system of 6 equations was solved using the function “fsolve” of Matlab (version
 890 R2013a, Mathworks). The steady state values were used as starting values for the
 891 numerical integration of the kinetic equations using the “ode15s” function of Matlab
 892 (version R2013a, Mathworks).

893 For parameter optimization, model simulations were compared to experimental
 894 capacitance data. The parameters of the model were varied and the goodness of fit
 895 was determined in a cost function, which was the sum of squared deviations between
 896 data and model prediction. In order to avoid bias towards data with larger secretion,
 897 the cost function used relative deviations: deviations were normalized to the maximal
 898 value of either the experimental capacitance trace or the simulated one, whichever
 899 was smaller (led to a larger cost):

$$cost = \frac{weight(i)}{\max(y_{Experiment})} \sum_i (y_{Experiment}(i) - y_{Model}(i))^2 \quad \text{for } \max(y_{Experiment}) < \max(y_{Model})$$

$$cost = \frac{weight(i)}{\max(y_{Model})} \sum_i (y_{Experiment}(i) - y_{Model}(i))^2 \quad \text{for } \max(y_{Experiment}) \geq \max(y_{Model})$$

900

901 Three principal kinetic components have been described in capacitance traces: a fast
 902 component with a time constant of tens of milliseconds, a slower component with a
 903 time constant of hundreds of milliseconds and a sustained component with a time
 904 constant of several seconds (Voets, 2000). To account for the fact that more data
 905 points exist for slower components (due to the constant sampling rate) which would
 906 dominate the fit, deviations at shorter times after the uncaging flash were given larger
 907 weight: the weight was 100 for all datapoints upto 80 ms after the uncaging stimulus;
 908 the weight was 10 for all datapoints occurring later than 80 ms, but earlier than 1.2 s
 909 after the stimulus; the weight was 1 for all datapoints thereafter. To ensure
 910 consistency, all conditions depicted in Figure 7 were fitted simultaneously and the
 911 cost values from all data were summed. Only the parameters labeled with “best fit” in
 912 Table 1 were allowed to vary. Because the lowest bin of the capacitance traces of the
 913 DKO overexpressing Munc13-1 and ubMunc13-2 in Figure 7B and C contained
 914 relatively few cells, the total number of vesicles was also a free parameter under these
 915 conditions (best fit values $V_{tot}(\text{Munc13-1 low } Ca^{2+})=2120$ fF, $V_{tot}(\text{Munc13-1 low } Ca^{2+})=3340$ fF). All parameters were optimized by minimizing the cost values using a

917 Nelder-Mead Simplex algorithm implemented in the Matlab function “fminsearch”
918 (version R2013a, Mathworks).

919

920 **Statistics**

921 Statistical analyses were performed using two-tailed Student’s *t*-test, ANOVA with
922 post-hoc Tukey’s test, or Mann-Whitney U test as specified in the figure legends.

923

924 **Acknowledgements**

925 This work was supported by the Max Planck Society. K-M.M. was supported by the
926 German Academic Exchange Service and the Göttingen Graduate School for
927 Neurosciences, Biophysics and Molecular Biosciences. A.W. was supported by the
928 Emmy Noether Program of the Deutsche Forschungsgemeinschaft. The work was
929 supported by The Danish Council for Independent Research in Medical Sciences
930 (J.B.S.). We thank J.-S. Rhee for advice, A. Zeuch, A. Günther, I. Beulshausen, S.
931 Bolte, F. Benseler, I. Thanhäuser, D. Schwerdtfeger, C. Harenberg, and M. Schlieper
932 for excellent technical support, and the MPIEM animal facility for mouse husbandry.

933 The authors declare no competing financial interests.

934 Author contributions: K-M.M., C.I., J.S., B.C., N.B. and S.W. designed research; K-
935 M.M., C.I., A.W., P.P. and B.C. performed research; K-M.M., C.I., A.W., P.P., D.S.,
936 J.R., J.S. and S.W. analyzed data; K-M.M., C.I., A.W., J.S., N.B. and S.W. wrote the
937 paper.

938
939

940 **References**

941

942 Ashery, U., A. Betz, T. Xu, N. Brose, and J. Rettig. 1999. An efficient method for
943 infection of adrenal chromaffin cells using the Semliki Forest virus gene
944 expression system. *Eur. J. Cell Biol.* 78:525-532.

945 Ashery, U., F. Varoqueaux, T. Voets, A. Betz, P. Thakur, H. Koch, E. Neher, N.
946 Brose, and J. Rettig. 2000. Munc13-1 acts as a priming factor for large dense-
947 core vesicles in bovine chromaffin cells. *EMBO J.* 19:3586-3596.

948 Augustin, I., S. Korte, M. Rickmann, H.A. Kretzschmar, T.C. Sudhof, J.W. Herms,
949 and N. Brose. 2001. The cerebellum-specific Munc13 isoform Munc13-3
950 regulates cerebellar synaptic transmission and motor learning in mice. *J.*
951 *Neurosci.* 21:10-17.

952 Augustin, I., C. Rosenmund, T.C. Sudhof, and N. Brose. 1999. Munc13-1 is essential
953 for fusion competence of glutamatergic synaptic vesicles. *Nature.* 400:457-
954 461.

955 Bauer, C.S., R.J. Woolley, A.G. Teschemacher, and E.P. Seward. 2007. Potentiation
956 of exocytosis by phospholipase C-coupled G-protein-coupled receptors
957 requires the priming protein Munc13-1. *J. Neurosci.* 27:212-219.

958 Borisovska, M., Y. Zhao, Y. Tsytsyura, N. Glyvuk, S. Takamori, U. Matti, J. Rettig,
959 T. Sudhof, and D. Bruns. 2005. v-SNAREs control exocytosis of vesicles from
960 priming to fusion. *EMBO J.* 24:2114-2126.

961 Boswell, K.L., D.J. James, J.M. Esquibel, S. Bruinsma, R. Shirakawa, H. Horiuchi,
962 and T.F. Martin. 2012. Munc13-4 reconstitutes calcium-dependent SNARE-
963 mediated membrane fusion. *J. Cell Biol.* 197:301-312.

964 Bruns, D. 2004. Detection of transmitter release with carbon fiber electrodes.
965 *Methods.* 33:312-321.

966 Cooper, B., M. Hemmerlein, J. Ammermuller, C. Imig, K. Reim, N. Lipstein, S.
967 Kalla, H. Kawabe, N. Brose, J.H. Brandstatter, and F. Varoqueaux. 2012.
968 Munc13-independent vesicle priming at mouse photoreceptor ribbon synapses.
969 *J. Neurosci.* 32:8040-8052.

970 Crozat, K., K. Hoebe, S. Ugolini, N.A. Hong, E. Janssen, S. Rutschmann, S. Mudd, S.
971 Sovath, E. Vivier, and B. Beutler. 2007. Jinx, an MCMV susceptibility
972 phenotype caused by disruption of Unc13d: a mouse model of type 3 familial
973 hemophagocytic lymphohistiocytosis. *J. Exp. Med.* 204:853-863.

974 Daily, N.J., K.L. Boswell, D.J. James, and T.F. Martin. 2010. Novel interactions of
975 CAPS (Ca²⁺-dependent activator protein for secretion) with the three
976 neuronal SNARE proteins required for vesicle fusion. *J. Biol. Chem.*
977 285:35320-35329.

978 de Wit, H. 2010. Molecular mechanism of secretory vesicle docking. *Biochem. Soc.*
979 *Trans.* 38:192-198.

- 980 de Wit, H., L.N. Cornelisse, R.F. Toonen, and M. Verhage. 2006. Docking of
981 secretory vesicles is syntaxin dependent. *PLoS One*. 1:e126.
- 982 de Wit, H., A.M. Walter, I. Milosevic, A. Gulyas-Kovacs, D. Riedel, J.B. Sorensen,
983 and M. Verhage. 2009. Synaptotagmin-1 docks secretory vesicles to syntaxin-
984 1/SNAP-25 acceptor complexes. *Cell*. 138:935-946.
- 985 Elhamdani, A., T.F. Martin, J.A. Kowalchyk, and C.R. Artalejo. 1999. Ca(2+)-
986 dependent activator protein for secretion is critical for the fusion of dense-core
987 vesicles with the membrane in calf adrenal chromaffin cells. *J. Neurosci*.
988 19:7375-7383.
- 989 Fasshauer, D., and M. Margittai. 2004. A transient N-terminal interaction of SNAP-25
990 and syntaxin nucleates SNARE assembly. *J. Biol. Chem*. 279:7613-7621.
- 991 Feldmann, J., I. Callebaut, G. Raposo, S. Certain, D. Bacq, C. Dumont, N. Lambert,
992 M. Ouachee-Chardin, G. Chedeville, H. Tamary, V. Minard-Colin, E. Vilmer,
993 S. Blanche, F. Le Deist, A. Fischer, and G. de Saint Basile. 2003. Munc13-4 is
994 essential for cytolytic granules fusion and is mutated in a form of familial
995 hemophagocytic lymphohistiocytosis (FHL3). *Cell*. 115:461-473.
- 996 Gandasi, N.R., and S. Barg. 2014. Contact-induced clustering of syntaxin and munc18
997 docks secretory granules at the exocytosis site. *Nat. Commun*. 5:3914.
- 998 Gao, Y., S. Zorman, G. Gundersen, Z. Xi, L. Ma, G. Sirinakis, J.E. Rothman, and Y.
999 Zhang. 2012. Single reconstituted neuronal SNARE complexes zipper in three
1000 distinct stages. *Science*. 337:1340-1343.
- 1001 Gerber, S.H., J.C. Rah, S.W. Min, X. Liu, H. de Wit, I. Dulubova, A.C. Meyer, J.
1002 Rizo, M. Arancillo, R.E. Hammer, M. Verhage, C. Rosenmund, and T.C.
1003 Sudhof. 2008. Conformational switch of syntaxin-1 controls synaptic vesicle
1004 fusion. *Science*. 321:1507-1510.
- 1005 Graham, M.E., M.T. Handley, J.W. Barclay, L.F. Ciufo, S.L. Barrow, A. Morgan, and
1006 R.D. Burgoyne. 2008. A gain-of-function mutant of Munc18-1 stimulates
1007 secretory granule recruitment and exocytosis and reveals a direct interaction of
1008 Munc18-1 with Rab3. *Biochem. J*. 409:407-416.
- 1009 Gulyas-Kovacs, A., H. de Wit, I. Milosevic, O. Kochubey, R. Toonen, J. Klingauf, M.
1010 Verhage, and J.B. Sorensen. 2007. Munc18-1: sequential interactions with the
1011 fusion machinery stimulate vesicle docking and priming. *J. Neurosci*.
1012 27:8676-8686.
- 1013 Hammarlund, M., M.T. Palfreyman, S. Watanabe, S. Olsen, and E.M. Jorgensen.
1014 2007. Open syntaxin docks synaptic vesicles. *PLoS Biol*. 5:e198.
- 1015 Hammarlund, M., S. Watanabe, K. Schuske, and E.M. Jorgensen. 2008. CAPS and
1016 syntaxin dock dense core vesicles to the plasma membrane in neurons. *J. Cell*
1017 *Biol*. 180:483-491.
- 1018 Han, G.A., N.T. Malintan, N.M. Saw, L. Li, L. Han, F.A. Meunier, B.M. Collins, and
1019 S. Sugita. 2011. Munc18-1 domain-1 controls vesicle docking and secretion

- 1020 by interacting with syntaxin-1 and chaperoning it to the plasma membrane.
1021 *Mol. Biol. Cell.* 22:4134-4149.
- 1022 Honigmann, A., G. van den Bogaart, E. Iraheta, H.J. Risselada, D. Milovanovic, V.
1023 Mueller, S. Mullar, U. Diederichsen, D. Fasshauer, H. Grubmuller, S.W. Hell,
1024 C. Eggeling, K. Kuhnel, and R. Jahn. 2013. Phosphatidylinositol 4,5-
1025 bisphosphate clusters act as molecular beacons for vesicle recruitment. *Nat.*
1026 *Struct. Mol. Biol.* 20:679-686.
- 1027 Imig, C., S.W. Min, S. Krinner, M. Arancillo, C. Rosenmund, T.C. Südhof, J.S. Rhee,
1028 N. Brose, and B.H. Cooper. 2014. The morphological and molecular nature of
1029 synaptic vesicle priming at presynaptic active zones. *Neuron.* 82:416-431.
- 1030 James, D.J., and T.F. Martin. 2013. CAPS and Munc13: CATCHRs that SNARE
1031 Vesicles. *Front. Endocrinol. (Lausanne).* 4:187.
- 1032 Jockusch, W.J., D. Speidel, A. Sigler, J.B. Sorensen, F. Varoqueaux, J.S. Rhee, and
1033 N. Brose. 2007. CAPS-1 and CAPS-2 are essential synaptic vesicle priming
1034 proteins. *Cell.* 131:796-808.
- 1035 Kabachinski, G., M. Yamaga, D.M. Kielar-Grevstad, S. Bruinsma, and T.F. Martin.
1036 2014. CAPS and Munc13 utilize distinct PIP2-linked mechanisms to promote
1037 vesicle exocytosis. *Mol. Biol. Cell.* 25:508-521.
- 1038 Kalla, S., M. Stern, J. Basu, F. Varoqueaux, K. Reim, C. Rosenmund, N.E. Ziv, and
1039 N. Brose. 2006. Molecular dynamics of a presynaptic active zone protein
1040 studied in Munc13-1-enhanced yellow fluorescent protein knock-in mutant
1041 mice. *J. Neurosci.* 26:13054-13066.
- 1042 Kang, L., Z. He, P. Xu, J. Fan, A. Betz, N. Brose, and T. Xu. 2006. Munc13-1 is
1043 required for the sustained release of insulin from pancreatic beta cells. *Cell.*
1044 *Metab.* 3:463-468.
- 1045 Koch, H., K. Hofmann, and N. Brose. 2000. Definition of Munc13-homology-
1046 domains and characterization of a novel ubiquitously expressed Munc13
1047 isoform. *Biochem. J.* 349:247-253.
- 1048 Kremer, J.R., D.N. Mastrorarde, and J.R. McIntosh. 1996. Computer visualization of
1049 three-dimensional image data using IMOD. *J. Struct. Biol.* 116:71-76.
- 1050 Kwan, E.P., L. Xie, L. Sheu, C.J. Nolan, M. Prentki, A. Betz, N. Brose, and H.Y.
1051 Gaisano. 2006. Munc13-1 deficiency reduces insulin secretion and causes
1052 abnormal glucose tolerance. *Diabetes.* 55:1421-1429.
- 1053 Lecat, S., H.W. Matthes, R. Pepperkok, J.C. Simpson, and J.L. Galzi. 2015. A
1054 Fluorescent Live Imaging Screening Assay Based on Translocation Criteria
1055 Identifies Novel Cytoplasmic Proteins Implicated in G Protein-coupled
1056 Receptor Signaling Pathways. *Mol. Cell. Proteomics.* 14:1385-1399.
- 1057 Liu, Y., C. Schirra, L. Edelmann, U. Matti, J. Rhee, D. Hof, D. Bruns, N. Brose, H.
1058 Rieger, D.R. Stevens, and J. Rettig. 2010. Two distinct secretory vesicle-
1059 priming steps in adrenal chromaffin cells. *J. Cell Biol.* 190:1067-1077.

- 1060 Liu, Y., C. Schirra, D.R. Stevens, U. Matti, D. Speidel, D. Hof, D. Bruns, N. Brose,
1061 and J. Rettig. 2008. CAPS facilitates filling of the rapidly releasable pool of
1062 large dense-core vesicles. *J. Neurosci.* 28:5594-5601.
- 1063 Ma, C., W. Li, Y. Xu, and J. Rizo. 2011. Munc13 mediates the transition from the
1064 closed syntaxin-Munc18 complex to the SNARE complex. *Nat. Struct. Mol.*
1065 *Biol.* 18:542-549.
- 1066 Ma, C., L. Su, A.B. Seven, Y. Xu, and J. Rizo. 2013. Reconstitution of the vital
1067 functions of Munc18 and Munc13 in neurotransmitter release. *Science.*
1068 339:421-425.
- 1069 Mastronarde, D.N. 2005. Automated electron microscope tomography using robust
1070 prediction of specimen movements. *J. Struct. Biol.* 152:36-51.
- 1071 Mobius, W., B. Cooper, W.A. Kaufmann, C. Imig, T. Ruhwedel, N. Snaidero, A.S.
1072 Saab, and F. Varoqueaux. 2010. Electron microscopy of the mouse central
1073 nervous system. *Methods Cell Biol.* 96:475-512.
- 1074 Moser, T., and E. Neher. 1997. Rapid exocytosis in single chromaffin cells recorded
1075 from mouse adrenal slices. *J. Neurosci.* 17:2314-2323.
- 1076 Mosharov, E.V., and D. Sulzer. 2005. Analysis of exocytotic events recorded by
1077 amperometry. *Nat. Methods.* 2:651-658.
- 1078 Neher, E. 2006. A comparison between exocytic control mechanisms in adrenal
1079 chromaffin cells and a glutamatergic synapse. *Pflugers Arch.* 453:261-268.
- 1080 Ovsepian, S.V., and J.O. Dolly. 2011. Dendritic SNAREs add a new twist to the old
1081 neuron theory. *Proc. Natl. Acad. Sci. U. S. A.* 108:19113-19120.
- 1082 Pang, Z.P., and T.C. Sudhof. 2010. Cell biology of Ca²⁺-triggered exocytosis. *Curr.*
1083 *Opin. Cell Biol.* 22:496-505.
- 1084 Parisotto, D., J. Malsam, A. Scheutzow, J.M. Krause, and T.H. Sollner. 2012.
1085 SNAREpin assembly by Munc18-1 requires previous vesicle docking by
1086 synaptotagmin 1. *J. Biol. Chem.* 287:31041-31049.
- 1087 Park, Y., J.B. Seo, A. Fraind, A. Perez-Lara, H. Yavuz, K. Han, S.R. Jung, I. Kattan,
1088 P.J. Walla, M. Choi, D.S. Cafiso, D.S. Koh, and R. Jahn. 2015.
1089 Synaptotagmin-1 binds to PIP₂-containing membrane but not to SNAREs at
1090 physiological ionic strength. *Nat. Struct. Mol. Biol.* 22:815-823.
- 1091 Parsons, T.D., J.R. Coorssen, H. Horstmann, and W. Almers. 1995. Docked granules,
1092 the exocytic burst, and the need for ATP hydrolysis in endocrine cells.
1093 *Neuron.* 15:1085-1096.
- 1094 Pinheiro, P.S., A.M. Jansen, H. de Wit, B. Tawfik, K.L. Madsen, M. Verhage, U.
1095 Gether, and J.B. Sorensen. 2014. The BAR domain protein PICK1 controls
1096 vesicle number and size in adrenal chromaffin cells. *J. Neurosci.* 34:10688-
1097 10700.

- 1098 Plattner, H., A.R. Artalejo, and E. Neher. 1997. Ultrastructural organization of bovine
1099 chromaffin cell cortex-analysis by cryofixation and morphometry of aspects
1100 pertinent to exocytosis. *J. Cell Biol.* 139:1709-1717.
- 1101 Pobbati, A.V., A. Stein, and D. Fasshauer. 2006. N- to C-terminal SNARE complex
1102 assembly promotes rapid membrane fusion. *Science.* 313:673-676.
- 1103 Renden, R., B. Berwin, W. Davis, K. Ann, C.T. Chin, R. Kreber, B. Ganetzky, T.F.
1104 Martin, and K. Broadie. 2001. Drosophila CAPS is an essential gene that
1105 regulates dense-core vesicle release and synaptic vesicle fusion. *Neuron.*
1106 31:421-437.
- 1107 Richmond, J.E., W.S. Davis, and E.M. Jorgensen. 1999. UNC-13 is required for
1108 synaptic vesicle fusion in *C. elegans*. *Nat. Neurosci.* 2:959-964.
- 1109 Rosenmund, C., A. Sigler, I. Augustin, K. Reim, N. Brose, and J.S. Rhee. 2002.
1110 Differential control of vesicle priming and short-term plasticity by Munc13
1111 isoforms. *Neuron.* 33:411-424.
- 1112 Rostaing, P., E. Real, L. Siksou, J.P. Lechaire, T. Boudier, T.M. Boeckers, F. Gertler,
1113 E.D. Gundelfinger, A. Triller, and S. Marty. 2006. Analysis of synaptic
1114 ultrastructure without fixative using high-pressure freezing and tomography.
1115 *Eur. J. Neurosci.* 24:3463-3474.
- 1116 Sassa, T., S. Harada, H. Ogawa, J.B. Rand, I.N. Maruyama, and R. Hosono. 1999.
1117 Regulation of the UNC-18-Caenorhabditis elegans syntaxin complex by UNC-
1118 13. *J. Neurosci.* 19:4772-4777.
- 1119 Schonn, J.S., J.R. van Weering, R. Mohrmann, O.M. Schluter, T.C. Sudhof, H. de
1120 Wit, M. Verhage, and J.B. Sorensen. 2010. Rab3 proteins involved in vesicle
1121 biogenesis and priming in embryonic mouse chromaffin cells. *Traffic.*
1122 11:1415-1428.
- 1123 Shirakawa, R., T. Higashi, A. Tabuchi, A. Yoshioka, H. Nishioka, M. Fukuda, T.
1124 Kita, and H. Horiuchi. 2004. Munc13-4 is a GTP-Rab27-binding protein
1125 regulating dense core granule secretion in platelets. *J. Biol. Chem.* 279:10730-
1126 10737.
- 1127 Siksou, L., F. Varoqueaux, O. Pascual, A. Triller, N. Brose, and S. Marty. 2009. A
1128 common molecular basis for membrane docking and functional priming of
1129 synaptic vesicles. *Eur. J. Neurosci.* 30:49-56.
- 1130 Sorensen, J.B., R. Fernandez-Chacon, T.C. Sudhof, and E. Neher. 2003a. Examining
1131 synaptotagmin 1 function in dense core vesicle exocytosis under direct control
1132 of Ca²⁺. *J. Gen. Physiol.* 122:265-276.
- 1133 Sorensen, J.B., G. Nagy, F. Varoqueaux, R.B. Nehring, N. Brose, M.C. Wilson, and
1134 E. Neher. 2003b. Differential control of the releasable vesicle pools by SNAP-
1135 25 splice variants and SNAP-23. *Cell.* 114:75-86.
- 1136 Sorensen, J.B., K. Wiederhold, E.M. Muller, I. Milosevic, G. Nagy, B.L. de Groot, H.
1137 Grubmuller, and D. Fasshauer. 2006. Sequential N- to C-terminal SNARE

- 1138 complex assembly drives priming and fusion of secretory vesicles. *EMBO J.*
1139 25:955-966.
- 1140 Speese, S., M. Petrie, K. Schuske, M. Ailion, K. Ann, K. Iwasaki, E.M. Jorgensen,
1141 and T.F. Martin. 2007. UNC-31 (CAPS) is required for dense-core vesicle but
1142 not synaptic vesicle exocytosis in *Caenorhabditis elegans*. *J. Neurosci.*
1143 27:6150-6162.
- 1144 Speidel, D., A. Salehi, S. Obermueller, I. Lundquist, N. Brose, E. Renstrom, and P.
1145 Rorsman. 2008. CAPS1 and CAPS2 regulate stability and recruitment of
1146 insulin granules in mouse pancreatic beta cells. *Cell. Metab.* 7:57-67.
- 1147 Stevens, D.R., Z.X. Wu, U. Matti, H.J. Junge, C. Schirra, U. Becherer, S.M. Wojcik,
1148 N. Brose, and J. Rettig. 2005. Identification of the minimal protein domain
1149 required for priming activity of Munc13-1. *Curr. Biol.* 15:2243-2248.
- 1150 Toonen, R.F., O. Kochubey, H. de Wit, A. Gulyas-Kovacs, B. Konijnenburg, J.B.
1151 Sorensen, J. Klingauf, and M. Verhage. 2006. Dissecting docking and
1152 tethering of secretory vesicles at the target membrane. *EMBO J.* 25:3725-
1153 3737.
- 1154 Tsuboi, T., and M. Fukuda. 2006. Rab3A and Rab27A cooperatively regulate the
1155 docking step of dense-core vesicle exocytosis in PC12 cells. *J. Cell Sci.*
1156 119:2196-2203.
- 1157 van de Bospoort, R., M. Farina, S.K. Schmitz, A. de Jong, H. de Wit, M. Verhage,
1158 and R.F. Toonen. 2012. Munc13 controls the location and efficiency of dense-
1159 core vesicle release in neurons. *J. Cell Biol.* 199:883-891.
- 1160 van Weering, J.R., R.F. Toonen, and M. Verhage. 2007. The role of Rab3a in
1161 secretory vesicle docking requires association/dissociation of guanidine
1162 phosphates and Munc18-1. *PLoS One.* 2:e616.
- 1163 Varoqueaux, F., A. Sigler, J.S. Rhee, N. Brose, C. Enk, K. Reim, and C. Rosenmund.
1164 2002. Total arrest of spontaneous and evoked synaptic transmission but
1165 normal synaptogenesis in the absence of Munc13-mediated vesicle priming.
1166 *Proc. Natl. Acad. Sci. U. S. A.* 99:9037-9042.
- 1167 Varoqueaux, F., M.S. Sons, J.J. Plomp, and N. Brose. 2005. Aberrant morphology
1168 and residual transmitter release at the Munc13-deficient mouse neuromuscular
1169 synapse. *Mol. Cell. Biol.* 25:5973-5984.
- 1170 Voets, T. 2000. Dissection of three Ca²⁺-dependent steps leading to secretion in
1171 chromaffin cells from mouse adrenal slices. *Neuron.* 28:537-545.
- 1172 Voets, T., E. Neher, and T. Moser. 1999. Mechanisms underlying phasic and
1173 sustained secretion in chromaffin cells from mouse adrenal slices. *Neuron.*
1174 23:607-615.
- 1175 Voets, T., R.F. Toonen, E.C. Brian, H. de Wit, T. Moser, J. Rettig, T.C. Sudhof, E.
1176 Neher, and M. Verhage. 2001. Munc18-1 promotes large dense-core vesicle
1177 docking. *Neuron.* 31:581-591.

- 1178 Walter, A.M., P.S. Pinheiro, M. Verhage, and J.B. Sorensen. 2013. A sequential
1179 vesicle pool model with a single release sensor and a Ca(2+)-dependent
1180 priming catalyst effectively explains Ca(2+)-dependent properties of
1181 neurosecretion. *PLoS Comput. Biol.* 9:e1003362.
- 1182 Walter, A.M., K. Wiederhold, D. Bruns, D. Fasshauer, and J.B. Sorensen. 2010.
1183 Synaptobrevin N-terminally bound to syntaxin-SNAP-25 defines the primed
1184 vesicle state in regulated exocytosis. *J. Cell Biol.* 188:401-413.
- 1185 Weimer, R.M., E.O. Gracheva, O. Meyrignac, K.G. Miller, J.E. Richmond, and J.L.
1186 Bessereau. 2006. UNC-13 and UNC-10/rim localize synaptic vesicles to
1187 specific membrane domains. *J. Neurosci.* 26:8040-8047.
- 1188 Wojcik, S.M., M. Tantra, B. Stepniak, K.N. Man, K. Muller-Ribbe, M. Begemann, A.
1189 Ju, S. Papiol, A. Ronnenberg, A. Gurvich, Y. Shin, I. Augustin, N. Brose, and
1190 H. Ehrenreich. 2013. Genetic markers of a Munc13 protein family member,
1191 BAIAP3, are gender specifically associated with anxiety and benzodiazepine
1192 abuse in mice and humans. *Mol. Med.* 19:135-148.
- 1193 Wu, Y., Y. Gu, M.K. Morphew, J. Yao, F.L. Yeh, M. Dong, and E.R. Chapman.
1194 2012. All three components of the neuronal SNARE complex contribute to
1195 secretory vesicle docking. *J. Cell Biol.* 198:323-330.
- 1196 Yang, X., S. Wang, Y. Sheng, M. Zhang, W. Zou, L. Wu, L. Kang, J. Rizo, R. Zhang,
1197 T. Xu, and C. Ma. 2015. Syntaxin opening by the MUN domain underlies the
1198 function of Munc13 in synaptic-vesicle priming. *Nat. Struct. Mol. Biol.*
1199 22:547-554.
- 1200 Zhou, K.M., Y.M. Dong, Q. Ge, D. Zhu, W. Zhou, X.G. Lin, T. Liang, Z.X. Wu, and
1201 T. Xu. 2007. PKA activation bypasses the requirement for UNC-31 in the
1202 docking of dense core vesicles from *C. elegans* neurons. *Neuron.* 56:657-669.
- 1203 Zhou, Z., and S. Mislser. 1995. Action potential-induced quantal secretion of
1204 catecholamines from rat adrenal chromaffin cells. *J. Biol. Chem.* 270:3498-
1205 3505.
- 1206 Zikich, D., A. Mezer, F. Varoqueaux, A. Sheinin, H.J. Junge, E. Nachliel, R.
1207 Melamed, N. Brose, M. Gutman, and U. Ashery. 2008. Vesicle priming and
1208 recruitment by ubMunc13-2 are differentially regulated by calcium and
1209 calmodulin. *J. Neurosci.* 28:1949-1960.
1210
1211
1212

1213 **Figure legends**

1214 **Figure 1.**

1215 **Expression of Munc13 isoforms in the mouse adrenal gland.** KO mouse lines of
1216 the respective Munc13 isoform were used as control. The antibodies used to detect
1217 individual Munc13 isoforms and loading controls are indicated on the left. **(A)**
1218 Munc13-1 (*) is barely detectable in perinatal adrenal gland. **(B)** ubMunc13-2, but not
1219 bMunc13-2, is expressed. **(C)** Munc13-3 was not detected. **(D)** Baiap3 was detected,
1220 but not **(E)** Munc13-4. *Jx* refers to mice homozygous for the *Unc13d*^{*Jinx*} mutation
1221 (Croizat et al., 2007). **(F)** Munc13-1 and Baiap3 are mainly located in the medulla
1222 (Med), but ubMunc13-2 is present in cortex (Cort) as well. Please note that the
1223 difference in the position of ubMunc13-2 relative to the marker in panels **(B)** and **(F)**
1224 is due to how far the respective gels were run. Loading controls were valosin-
1225 containing protein (VCP), glyceraldehyde-3-phosphate dehydrogenase (GAPDH) and
1226 CgA. Brain samples, and spleen tissue in the case of Munc13-4, were used for
1227 comparison. Please note that the *Baiap3*^{KO} (Wojcik et al., 2013) and *Unc13a*^{KO}
1228 animals express truncated protein products, whereas the truncated product present in
1229 the *Unc13b*^{KO} (Cooper et al., 2012) is not shown here. Based on previous analyses of
1230 the *Unc13a*^{KO} and *Unc13b*^{KO} mice (Augustin et al., 1999; Cooper et al., 2012;
1231 Varoqueaux et al., 2002), the truncated Munc13-1 and Munc13-2 products are neither
1232 functional, nor do they have a dominant-negative effect. The truncated Baiap3
1233 product was not detected in adrenal gland, and its effect in the brain, where it can be
1234 detected in young animals up to P21, is currently unknown (Wojcik et al., 2013). See
1235 also Figure 1–figure supplement 1.

1236

1237 **Figure 1–figure supplement 1.**

1238 **Comparison of Munc13-1, Munc13-2, and Munc13-3 expression.** (A) Adrenal
1239 gland and brain homogenates from *Unc13a*-EYFP, *Unc13b*-EYFP, and *Unc13c*-
1240 EGFP knockin (KI) mice were probed using an antibody that recognizes the GFP-
1241 derived tags, which allowed us to compare expression levels of Munc13-1,
1242 ubMunc13-2, bMunc13-2 and Munc13-3 with the same antibody. The two bands
1243 detected in the *Unc13b*-EYFP KI brain sample represent ubMunc13-2 (lower band)
1244 and bMunc13-2 (upper band). While all isoforms were detected in brain, ubMunc13-
1245 2-EYFP was the only isoform readily detectable in the adrenal gland. Valosin-
1246 containing protein (VCP) was used as a loading control. (B) Adrenal gland and brain
1247 samples from *Unc13a*^{KO}*Unc13b*^{KO} (DKO) mice and WT controls, probed with
1248 antibodies to Munc13-1, ubMunc13-2 and VCP as a loading control. Expression of
1249 Munc13-1 (marked with *, to distinguish it from co-migrating bands of higher
1250 molecular weight) is low in E18 adrenal glands, while ubMunc13-2 can be readily
1251 detected. The expression of both isoforms was abrogated in DKO mice. Please note
1252 that, like the single KO lines, the DKO animals express truncated Munc13-1 protein
1253 products and a truncated Munc13-2 product (Cooper et al., 2012), the latter is not
1254 shown here.

1255

1256 **Figure 2.**

1257 **Flash photolysis induced LDCV exocytosis in chromaffin cells.** For each KO line,
1258 the average intracellular $[Ca^{2+}] \pm SEM$ and the average ΔC_m are shown in panels (A-
1259 C, and E). Single gene deletions of (A) *Unc13a*, (B) *Unc13c*, or (C) *Baiap3* did not
1260 impair LDCV exocytosis. (D) Summary of burst sizes, sustained release rates, and

1261 time constants. **(E)** LDCV exocytosis is dramatically reduced in *Unc13a*^{KO}*Unc13b*^{KO}
1262 cells, *Unc13a*^{WT}*Unc13b*^{KO} cells, and *Unc13a*^{Het}*Unc13b*^{KO} cells. This reduction is
1263 primarily due to the absence of ubMunc13-2. **(F)** Fast burst, slow burst and the rate of
1264 sustained release are reduced in the absence of Munc13-1 and ubMunc13-2, as well as
1265 in the absence of ubMunc13-2 alone (ANOVA with post-hoc Tukey's test). **(G)**
1266 Compared to *Unc13a*^{WT}*Unc13b*^{KO} cells, the deletion of Munc13-1 causes significant
1267 reductions in the slow burst and the rate of sustained release (Student's *t*-test, two-
1268 tailed). **(H)** Delay of the onset of exocytosis after the flash stimulus (ANOVA with
1269 post-hoc Tukey's test). **(I)** Normalized traces show identical release kinetics of the
1270 exocytotic burst. **(J)** Summary of the release components shown in panels **(E, F, G)**.
1271 Time constants are not significantly different (ANOVA with post-hoc Tukey's test).
1272 ($p < 0.05$: *, $p < 0.01$: **, $p < 0.001$: ***). See also Figure 2–figure supplement 1.

1273

1274 **Figure 2–figure supplement 1.**

1275 **Single gene deletion or overexpression of Baiap3 does not affect LDCV**
1276 **exocytosis in chromaffin cells.** **(A)** LDCV exocytosis was elicited by a series of
1277 depolarizing steps to analyze the Immediately-Releasable Pool (IRP) of vesicles
1278 localized in the vicinity of Ca²⁺ channels and the Readily-Releasable Pool (RRP).
1279 Shown are the averaged [Ca²⁺] ± SEM, ΔCm, and whole-cell current traces. The inset
1280 in the whole-cell current panel shows an enlargement of the first 100 ms
1281 depolarization. **(B)** The size of the IRP, estimated based on the release elicited by 6
1282 short (10 ms) depolarization pulses, was not altered. **(C)** The total ΔCm caused by the
1283 depolarization train was also not altered in *Baiap3*^{KO} cells. Note that the data from
1284 *Baiap3*^{KO} and *Baiap3*^{WT} were matched for equal ionic influx according to the ionic

1285 charge of the first 100 ms depolarization to eliminate effects of differential ionic
1286 influx. **(D)** Overexpression (OE) of *Baiap3* in WT chromaffin cells. EGFP expression
1287 in WT cells was used as control. Shown are the averaged $[Ca^{2+}] \pm SEM$ and ΔC_m
1288 traces. **(E)** Burst sizes, rate of sustained release and the kinetics of release were not
1289 altered by the overexpression of *Baiap3* (Student's *t*-test, two-tailed). **(F)** Normalized
1290 traces of *Baiap3*^{WT} and *Baiap3*^{KO} cells overlapped with each other, indicating no
1291 alterations in release kinetics in *Baiap3*^{KO} cells.

1292

1293 **Figure 3.**

1294 **Absence of Munc13-2 results in a significant release deficit in response to**
1295 **depolarization.** **(A)** Shown are the averaged $[Ca^{2+}] \pm SEM$, ΔC_m , and whole-cell
1296 current traces of *Unc13b*^{WT} and *Unc13b*^{KO} cells. The inset in the whole-cell current
1297 panel shows an enlargement of the first 100 ms depolarization. **(B)** ΔC_m elicited by
1298 individual depolarizations was significantly different between the two groups. RRP,
1299 Readily-releasable Pool; IRP, Immediately-Releasable Pool. **(C)** The size of the RRP
1300 was measured as the ΔC_m after the train of depolarization pulses and was
1301 significantly reduced in *Unc13b*^{KO} cells. ($p < 0.05$: *, $p < 0.01$: **, $p < 0.001$: ***;
1302 Student's *t*-test, two-tailed).

1303

1304 **Figure 4.**

1305 **Reduced number of fusion events of catecholamine-containing LDCVs in the**
1306 **absence of Munc13-2.** **(A)** Illustration of a single amperometric spike, corresponding
1307 to the release of catecholamines from a single LDCV, and the parameters analyzed.

1308 (B) Representative amperometric recordings of a *Unc13b*^{WT} and a *Unc13b*^{KO} cell. (C)
1309 Dramatic reduction in spike frequency in *Unc13b*^{KO} chromaffin cells. (D) Spike
1310 duration, (E) width at half amplitude ($t_{1/2}$), (F) maximum spike amplitude, (G)
1311 amperometric charge, (H) rise time, and (I) decay time were unchanged in the
1312 *Unc13b*^{KO}. The stability of fusion pores was also not altered, as shown by the
1313 unchanged (J) foot amplitude, (K) duration and (L) charge. (M) The fraction of
1314 amperometric spikes with a detectable foot was reduced in *Unc13b*^{KO} cells. ($p <$
1315 0.05 :*, $p < 0.001$:***; Student's t -test, two-tailed).

1316

1317 **Figure 5.**

1318 **LDCV exocytosis in *Unc13a*^{KO}*Unc13b*^{KO} chromaffin cells is rescued by**
1319 **overexpression (OE) of Munc13-1, ubMunc13-2 and Munc13-4, but not Baiap3.**

1320 *Unc13a*^{KO}*Unc13b*^{KO} cells were infected with SFV-Munc13-1-EGFP, SFV-
1321 ubMunc13-2-EGFP, SFV-Munc13-4-IRES-EGFP or SFV-Baiap3-IRES-EGFP using
1322 SFV-EGFP as control. (A) Averaged $[Ca^{2+}] \pm SEM$ and capacitance traces ΔC_m are
1323 shown in the same graph to compare the efficiency of rescue: ubMunc13-2 >
1324 Munc13-1 > Munc13-4 > Baiap3. (B) Burst sizes and rates of sustained release after
1325 analysis of individual traces. ($p < 0.05$: *, $p < 0.001$: ***; Student's t -test, two-tailed).

1326 See Figure 5–figure supplement 1 for a direct comparison of Munc13-1-EGFP and
1327 ubMunc13-2-EGFP expressing cell matched for fluorescence intensity and Figure 5–
1328 figure supplement 2 for Western blotting to confirm the expression of Munc13-4 and
1329 Baiap3 from the IRES-constructs.

1330

1331 **Figure 5—figure supplement 1.**

1332 **Direct comparison of Munc13-1 and ubMunc13-2 over-expressing cells with**
1333 **matching EGFP fluorescence. (A)** Averaged $[Ca^{2+}] \pm SEM$ and capacitance traces
1334 ΔC_m are shown in the same graph to compare the efficiency of rescue. **(B)**
1335 Fluorescence intensity in arbitrary units (a.u.) of *Unc13a*^{KO}*Unc13b*^{KO} chromaffin
1336 cells over-expressing Munc13-1-EGFP and ubMunc13-2-EGFP. **(C)** Expression of
1337 ubMunc13-2 resulted in a significantly larger enhancement of burst size and rate of
1338 sustained release than expression of Munc13-1. ($p < 0.01$: **, $p < 0.001$: ***;
1339 Student's *t*-test, two-tailed).

1340

1341 **Figure 5—figure supplement 2.**

1342 **Western blot analysis confirming expression of Munc13-4 and Baiap3 SFV**
1343 **constructs.** Neuronal cultures were infected with SFV-Baiap3-IRES-EGFP and SFV-
1344 Munc13-4-IRES-EGFP, respectively. Tissue samples from *Baiap3* and *Unc13d* (Jx)
1345 WT and KO mice were used as controls. Both Baiap3 and Munc13-4 were expressed.
1346 Please note, that we had to use infected neurons for this analysis, because our
1347 chromaffin cell cultures do not provide enough material for Western blotting.

1348

1349 **Figure 6.**

1350 **Ultrastructural analysis of LDCV docking in adrenal chromaffin cells.** 2D-EM of
1351 **(A)** *Unc13a*^{Het}*Unc13b*^{Het} (CTRL) and **(B)** *Unc13a*^{KO}*Unc13b*^{KO} (DKO) adrenal glands.
1352 **(C)** Frequency distribution of LDCVs within 0-2 μm of the plasma membrane (PM).
1353 **(D)** Membrane-proximal LDCVs (0-40 nm of PM) normalized to PM circumference.

1354 (E) Total number of LDCVs normalized to cytoplasmic area. (F-K) Tomographically
1355 reconstructed subvolumes from 400 nm-thick sections through (F-H)
1356 *Unc13a^{Het}Unc13b^{Het}* and (I-K) *Unc13a^{KO}Unc13b^{KO}* cells in which docked LDCVs
1357 (enlarged in panels G, J) and undocked LDCVs (enlarged in panels H and K, small
1358 gaps separating undocked LDCVs from the PM indicated with arrowheads) can be
1359 distinguished. (L) Frequency distribution of membrane-proximal LDCVs distributed
1360 within 0-40 nm of the PM. (M) Number of membrane-proximal LDCVs expressed as
1361 a percentage of all LDCVs within 0-100 nm of the plasma membrane. (N) Percentage
1362 of docked LDCVs with respect to all membrane-proximal LDCVs (within 0-40 nm of
1363 PM). Scale bars represent 1 μ m in (A, B), 200 nm in (F, I), and 50 nm in (H, K). C:
1364 5779 LDCVs in CTRL and 4120 LDCVs in DKO profiles. D, E: CTRL: N=2, n=36; DKO:
1365 N=2; n=27. L: 473 LDCVs in CTRL and 386 LDCVs in DKO tomographic subvolumes.
1366 M, N: CTRL: N=2, n=24;DKO: N=2, n=26. Values indicate mean \pm SEM. (Student's *t*-
1367 test, two-tailed). See also Figure 6–figure supplement 1.

1368

1369 **Figure 6–figure supplement 1.**

1370 **Ultrastructural analysis of LDCV size in adrenal chromaffin cells.** 2D-EM of (A)
1371 *Unc13a^{Het}Unc13b^{Het}* (CTRL) and (B) *Unc13a^{KO}Unc13b^{KO}* (DKO) adrenal glands. (C)
1372 Frequency distribution of LDCV diameters measured by 3D-ET. (D) Mean LDCV
1373 diameter in randomly imaged chromaffin cell areas. (E) LDCV diameter of docked
1374 (0-4 nm of PM) vesicles. Scale bar in B represents 5 μ m. C: 846 LDCVs in CTRL and
1375 831 LDCVs in DKO tomographic subvolumes. D: CTRL: N=2, n=24; DKO: N=2,
1376 n=26. E: CTRL: N=2, n=98; DKO: N=2, n=140. Values indicate mean \pm SEM.

1377 (Student's t-test, two-tailed; diameters of docked LDCVs were tested with Mann-
1378 Whitney U test).

1379

1380 **Figure 7.**

1381 **Munc13-1 and ubMunc13-2 accelerate upstream vesicle priming (“priming step**
1382 **1”) with identical Ca^{2+} affinities, but distinct rates. (A) Estimation of steady-state**
1383 **Ca^{2+} affinities of vesicle priming driven by Munc13-1 or ubMunc13-2. Left two**
1384 **panels: binned and averaged secretory responses in $Unc13a^{\text{KO}}Unc13b^{\text{KO}}$ cells**
1385 **overexpressing (OE) either Munc13-1 (green) or ubMunc13-2 (blue). The release**
1386 **fraction at 30 ms (traces normalized to their amplitude after 3 s) after the stimulus was**
1387 **determined as the read-out for priming (vertical broken lines). Right panel: the**
1388 **fraction of release plotted as a function of pre-flash $[\text{Ca}^{2+}]$. Both genotypes are**
1389 **described by the same Hill function, suggesting a similar Ca^{2+} -dependence of priming**
1390 **(i.e. identical cooperativity and affinity). (B) Fits of a secretion model (see panel E) to**
1391 **the capacitance responses observed experimentally in $Unc13a^{\text{KO}}Unc13b^{\text{KO}}$ cells**
1392 **expressing Munc13-1 at intermediate and low pre-flash $[\text{Ca}^{2+}]$. Top panel: measured**
1393 **Ca^{2+} values were used to drive the secretion model. The chemical equation shows a**
1394 **priming sensor (PS), which is active in the Ca^{2+} bound state (Ca_nPS). The lower panel**
1395 **shows the experimental capacitance data (solid lines) together with simulations with**
1396 **the best fit parameters (broken lines; see Table 1). Insert: magnified view with**
1397 **horizontal/vertical scale bars: 200 ms/200 fF. (C) Same as (B), but for**
1398 **$Unc13a^{\text{KO}}Unc13b^{\text{KO}}$ cells expressing ubMunc13-2. The secretion model was fitted**
1399 **using identical K_{DPS} and n for the Ca^{2+} binding to the PS (determined by the analysis**
1400 **shown in panel A). The best-fit values suggest a ~2.5-fold slower on-rate (activation**

1401 rate), but a 4.5-fold higher maximal priming rate for ubMunc13-2 (see Table 1),
1402 resulting in a sigmoidal secretion response from low pre-flash $[Ca^{2+}]$. (D) Fitting our
1403 secretion model to the experimental data of several genotypes suggests that Munc13-1
1404 and ubMunc13-2 both primarily act by increasing the forward priming rate (k_1 , see
1405 also panel E), while loss of ubMunc13-2 – the dominant endogenous isoform – has
1406 the opposite effect. The downstream priming step (“priming 2”, k_2) changes in the
1407 opposite direction. (E) Secretion model: Munc13-1 (green) and ubMunc13-2 (blue)
1408 regulate the Ca^{2+} binding rates (k_{on}) to a PS, which controls the asymptotic forward
1409 priming rate k_1 (see text for details, Table 1 for fitted parameters, and Walter et al.,
1410 2013 for model development). NRP: Non-Releasable Pool; RRP: Readily-Releasable
1411 Pool; F: Fused pool. See also Figure 7–figure supplement 1.

1412

1413 **Figure 7–figure supplement 1.**

1414 **Exocytotic burst size as a function of pre-flash $[Ca^{2+}]$. *Unc13a^{KO}Unc13b^{KO}* cells**
1415 **were rescued by Munc13-1 or ubMunc13-2 overexpression (OE).** For ubMunc13-
1416 2, data from 23 cells already analyzed for Figure 5 were included here as well. The
1417 average size of the exocytotic burst is plotted as the ΔC_m 0.5 s after the flash stimulus
1418 \pm SEM against average pre-flash $[Ca^{2+}] \pm$ SEM. Cells were binned according to pre-
1419 flash $[Ca^{2+}]$. For *Munc13-1*, bins are 250-350 nM ($n = 17$), 350-450 nM ($n = 15$),
1420 450-550 nM ($n = 11$), 550-800 nM ($n = 11$), 800-1200 nM ($n = 13$), 1200-1700 nM (n
1421 $= 7$). For *ubMunc13-2*, bins are 250-350 nM ($n = 11$), 350-450 nM ($n = 20$), 450-540
1422 nM ($n = 10$), 540-800 nM ($n = 12$), 800-1200 nM ($n = 10$) and 1200-1700 nM ($n =$
1423 4).

1424

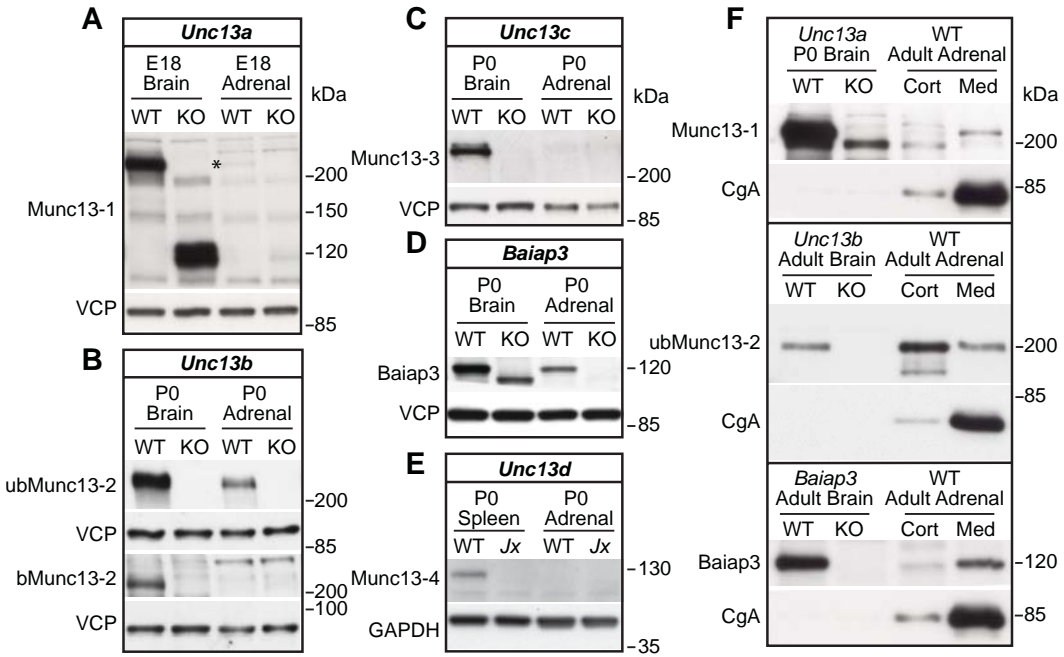
1425 Table 1. Parameters of the exocytosis model.

Parameter	Control	<i>Unc13b</i> ^{ko}	Munc13-1 OE	ubMunc13-2 OE	Comment
V_{tot}	2350				Total number of vesicles, best fit
k_1	$p(Ca^{2+}) \cdot k_{1max}$				
$p(Ca^{2+})$	$\frac{(Ca^{2+})^n}{(Ca^{2+})^n + (K_{D,cat})^n}$				fraction of activated PS
k_{on}	$8.96 \cdot 10^{-9} \text{ s}^{-1} \mu\text{M}^{-n}$	$2.25 \cdot 10^{-8} \text{ s}^{-1} \mu\text{M}^{-n}$	$2.25 \cdot 10^{-8} \text{ s}^{-1} \mu\text{M}^{-n}$	$8.96 \cdot 10^{-9} \text{ s}^{-1} \mu\text{M}^{-n}$	On-rate calcium binding to PS
k_{1Max}	$1.99 \cdot 10^{-2} \text{ s}^{-1}$	$6.89 \cdot 10^{-3} \text{ s}^{-1}$	$7.44 \cdot 10^{-2} \text{ s}^{-1}$	$3.42 \cdot 10^{-1} \text{ s}^{-1}$	Maximal priming rate, best fit
$\sqrt[n]{K_D}$	0.407 μM				Experiment, Hill plot Figure 7
k_{-1}	$4.70 \cdot 10^{-1} \text{ s}^{-1}$				Best fit
n	7.38				Cooperativity PS, experiment, Hill plot Figure 7
k_2	$= k_{20} + g(Ca^{2+}) \cdot k_{2cat}$				(Walter et al., 2013)
k_{-2}	$= k_{-20} + g(Ca^{2+}) \cdot k_{-2cat}$				(Walter et al., 2013)
$g(Ca^{2+})$	$\frac{Ca^{2+}}{Ca^{2+} + K_{D,cat}}$				(Walter et al., 2013)
k_{20}	$2.37 \cdot 10^{-2} \text{ s}^{-1}$	$2.95 \cdot 10^{-2} \text{ s}^{-1}$	$1.29 \cdot 10^{-2} \text{ s}^{-1}$	$5.80 \cdot 10^{-3} \text{ s}^{-1}$	Best fit
k_{2cat}	$3.95 \cdot 10^1 \text{ s}^{-1}$	$4.91 \cdot 10^1 \text{ s}^{-1}$	$2.14 \cdot 10^1 \text{ s}^{-1}$	$9.65 \cdot 10^0 \text{ s}^{-1}$	Best fit
k_{-20}	$2.10 \cdot 10^{-2} \text{ s}^{-1}$				Best fit
k_{-2cat}	$= k_{2cat} \cdot k_{-20} / k_{20}$				(Walter et al., 2013)
$K_{D, cat}$	138 μM				Best fit
k_3	$4.4 \text{ s}^{-1} \mu\text{M}^{-1}$				(Voets, 2000)
k_{-3}	56 s^{-1}				(Voets, 2000)
k_4	1450 s^{-1}				(Voets, 2000)

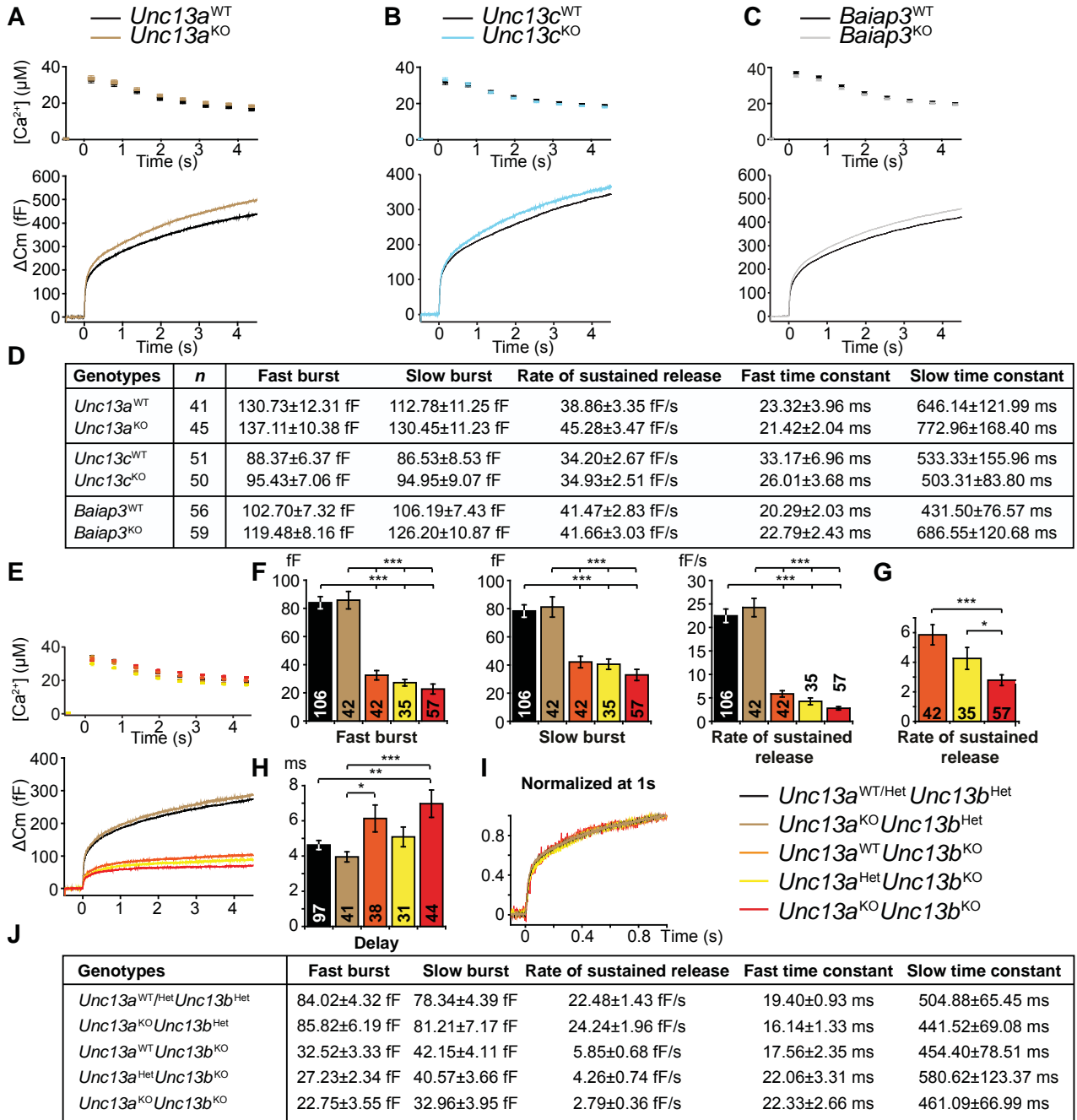
1426

1427

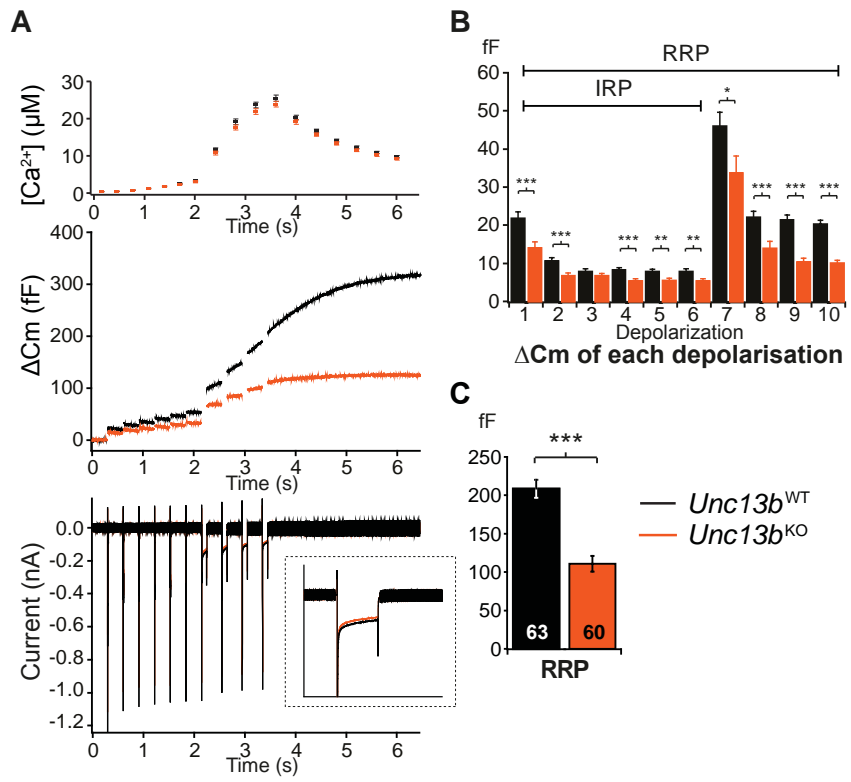
Man et al. Figure 1



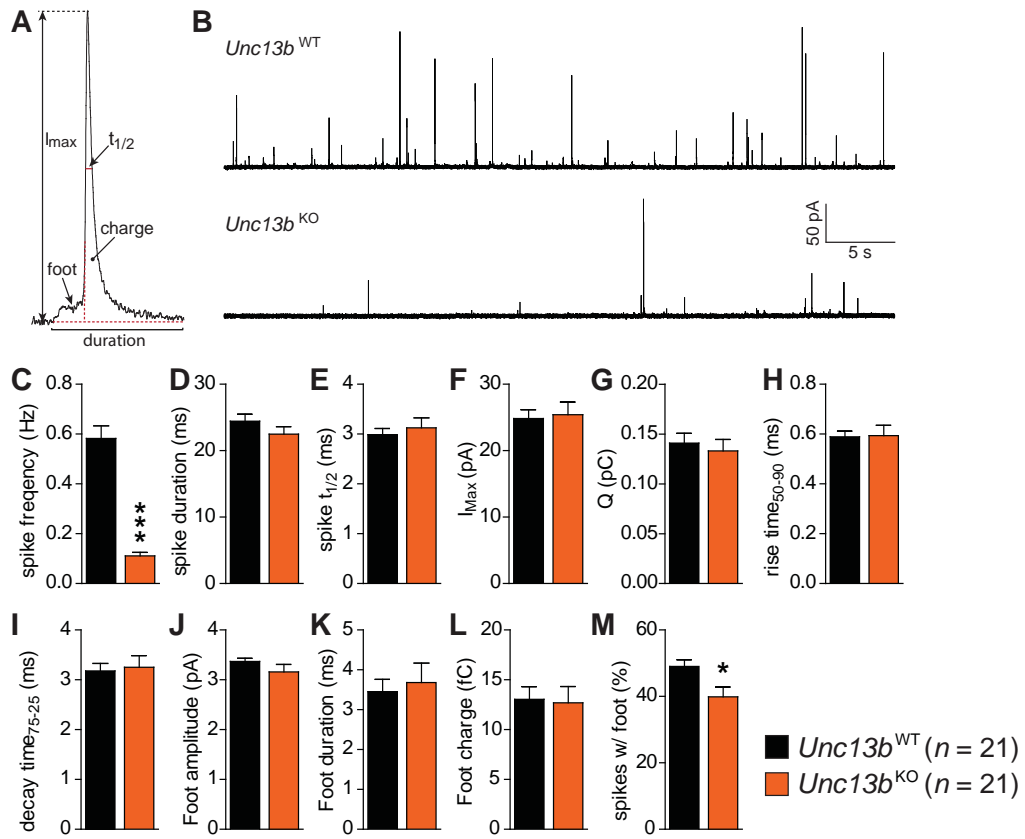
Man et al. Figure 2



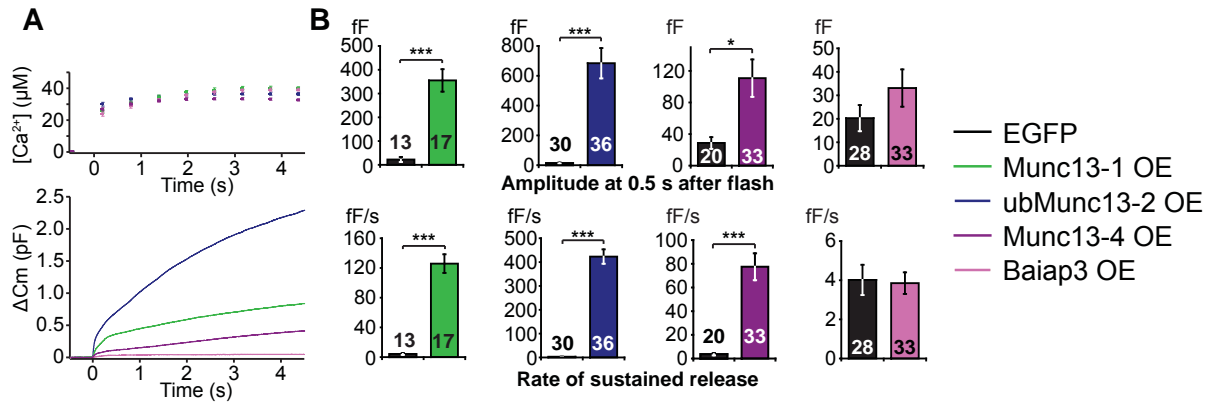
Man et al. Figure 3



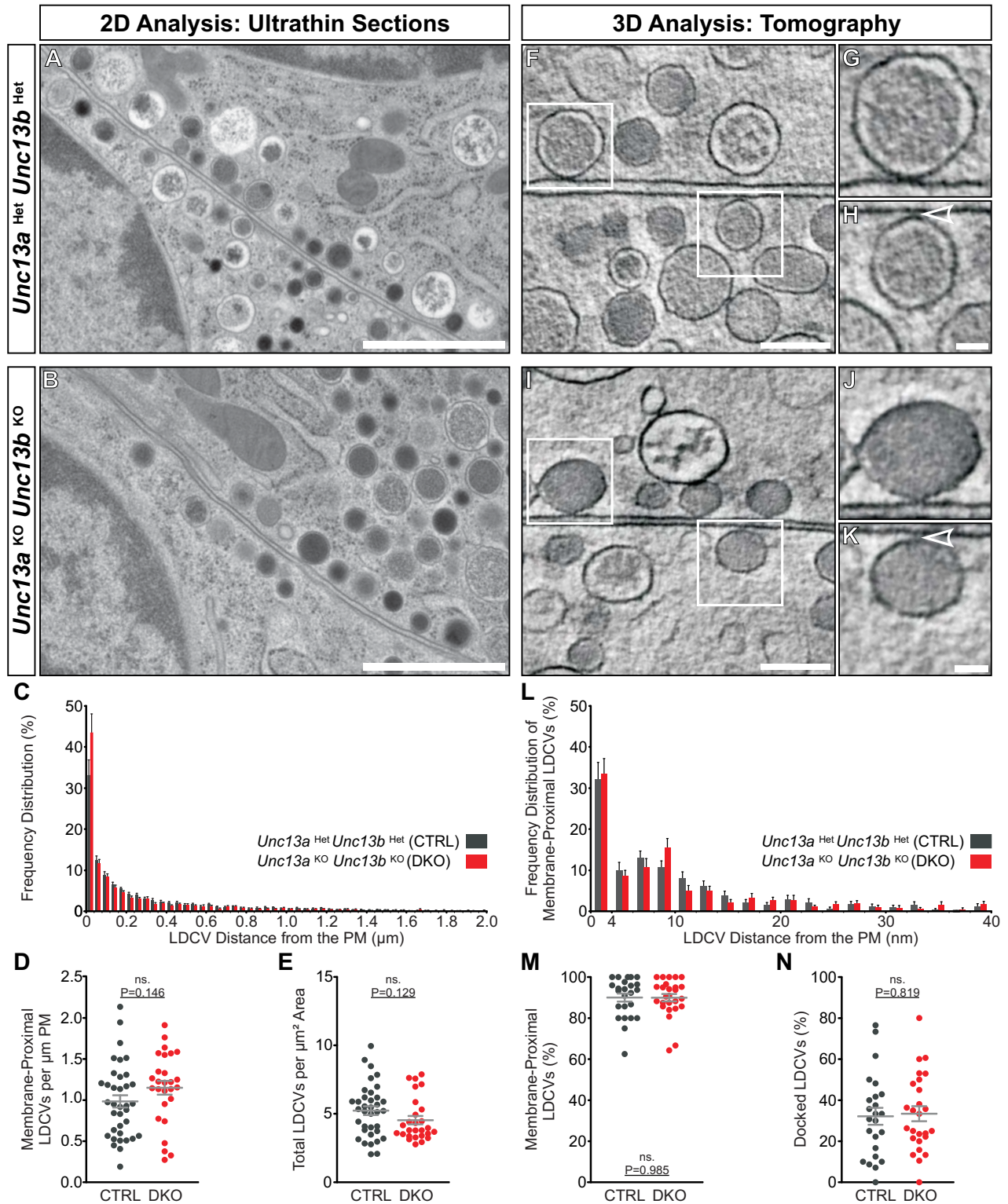
Man et al. Figure 4



Man et al. Figure 5



Man et al. Figure 6



Man et al. Figure 7

